Title page

Strategic Assembly of $La_{0.8}Sr_{0.2}CoO_3$ Nanoparticles into Supraparticles for Enhanced Oxygen Evolution in Alkaline Electrolysis

Mohaned Hammad[a,§]*, Blaž Toplak[a,§], Adil Amin[a], Mena-Alexander Kräenbring[a], Ahammed Suhail Odungat[a], Mohammed-Ali Sheikh[b], Adarsh Jain[a], Amin S. Amin[a], Ralf Meckenstock[d,e], Thai Binh Nguyen[c], Steven Angel[b], Michael Farle[d,e], Hartmut Wiggers[b,e], Doris Segets[a,e]*

[a] Institute for Energy and Materials Processes – Particle Science and Technology (EMPI–PST), University of Duisburg-Essen, Duisburg, Germany

[b] Institute for Energy and Materials Processes – Reactive Fluids (EMPI–RF), University of Duisburg-Essen, Duisburg, Germany

[c] Interdisciplinary Center for Analytics on the Nanoscale (ICAN), University of Duisburg-Essen, Duisburg, Germany

[d] Faculty of Physics, University of Duisburg-Essen, Duisburg, Germany

[e] Center for Nanointegration Duisburg-Essen (CENIDE), University of Duisburg-Essen, Duisburg, Germany

Corresponding author:
Dr. Mohaned Hammad*
Prof. Doris Segets*
Institute for Energy and Materials Processes – Particle Science and Technology
University of Duisburg-Essen
Carl-Benz-Str. 199
47057 Duisburg, Germany
mohaned.hammad@uni-due.de
doris.segets@uni-due.de
Tel: +49-(0)203-379 8230

[§] These authors contributed equally to this paper.

Abstract

Developing effective non-noble metal electrocatalysts for the oxygen evolution reaction (OER) remains challenging due to limited active sites and poor electronic conductivity in mixed oxide catalysts. To address these limitations, a one-step spray drying method is employed to synthesize hierarchical $La_{0.8}Sr_{0.2}CoO_3$ supraparticles (LSCO-SP) from high-surface-area nanoparticles (LSCO-NP). LSCO-SP demonstrate significantly enhanced OER performance, requiring ~300 mV lower overpotential at 100 mA cm^{-2} after 1 hour compared to LSCO-NP. Moreover, LSCO-SP exhibit faster catalytic kinetics, evidenced by a smaller Tafel slope of 76.2 mV dec^{-1} versus 82.5 mV dec^{-1} and lower charge transfer resistance of 1.11 Ω versus 1.31 Ω for LSCO-NP. The enhanced activity of LSCO-SP is attributed to their hierarchical porous architecture, which promotes efficient ion diffusion, improved electron transport, and increased accessibility to electroactive sites. Structural analyses confirmed that the LSCO-SP maintained their integrity under OER conditions. Furthermore, postmortem X-ray photoelectron spectroscopy and electron paramagnetic resonance analyses reveal a higher concentration of oxygen vacancies in LSCO-SP, suggesting that the supraparticle design tunes the lattice oxygen mechanism, enhancing OER performance. The hierarchical structure of LSCO-SP highlights their potential as a novel building block for catalyst layers in renewable energy applications.

Keywords: Perovskite nanomaterial; supraparticles; spray drying; porous structure; oxygen evolution reaction.

1 Introduction

The urgent issues of energy consumption and environmental pollution have increasingly driven the search for innovative energy conversion technologies, such as wind, solar, and fuel cells, along with various forms of energy storage like hydrogen and batteries [1,2]. Recently, the oxygen evolution reaction (OER) has gained particular importance in rechargeable metal-air batteries and water-splitting applications [3]. However, the OER is limited by sluggish kinetics due to the multiple proton-coupled electron transfer processes, leading to high overpotentials and significant energy losses [4]. Noble metal-based nanomaterials, such as ruthenium and iridium, are the most efficient OER catalysts for electrochemical water splitting, but their high cost and limited availability hinder their industrial application [5]. As a result, the demand for low-cost, highly efficient alternative catalysts has become increasingly significant. In this context, transition metal-based oxides have emerged as promising candidates due to their abundance, low cost, and high electrochemical activity [6]. However, the poor electrical conductivity of transition metal oxides, their instability under harsh conditions, and low accessibility of active sites remain major obstacles, limiting their performance during OER [7]. Consequently, recent efforts to overcome these challenges and improve their catalytic performance have included reducing nanoparticle sizes, introducing doping, and creating defect-rich surfaces [8,9]. In this regard, several transition metal alloys and their oxides-based nanocomposites such as CrCoNiFe [10], $Rb_{0.2}Sr_{0.8}Co_{0.4}Fe_{0.6}O_3$ [11], Fe_1Mn_1@nitrogen and boron co-doped carbon nanowires [12], and $NiFe_2O_4$@Ketjenblack carbon [13] amongst others, were successfully prepared. However, a reduced overpotential has been achieved only to a limited extent (up to 350 mV) and for short durations in rotating disk electrode configuration (about 2 h at 10 mA). Issues such as limited catalytic sites arising from low surface area, surface contamination, and aggregation of active sites over time, along with poor conductivity continue to slow down the progress in enhancing the catalytic efficiency over extended timeframes.

One promising approach to address these limitations involves constructing hierarchical structures, which accelerate electron transfer due to improved interparticle connectivity and promote higher accessibility of active sites by introducing porosity. The latter increases mass transfer characteristics, in particular bubble removal, while ideally eliminating diffusion limitations through optimized pore connectivity and structure. For instance, some reports have focused on synthesizing trimetallic (Fe, Co, Ni) spinel/carbon/nickel foam electrodes with 3D network structures for boosting the OER [14]. These hierarchical

superhydrophilic/superaerophobic pore networks exhibited a low overpotential of 221 mV at a current density of 10 mA cm^{-2} in 1 M KOH. The 3D network structures provide a high specific surface area and interconnected electron transfer. Furthermore, a previous report showed that a hierarchical framework of Ni/$NiFe_2O_4$@CNT microspheres prepared via spray drying exhibits a significantly improved OER performance compared to the traditional NiFe-based oxide or commercial RuO_2/IrO_2 [15]. The enhanced OER performance of the Ni/$NiFe_2O_4$@CNT composite is mainly attributed to the increased catalytic activity and the improved conductivity induced by the strong hierarchical coupling for a high connectivity and therefore resulting in enhanced charge transfer between CNTs and Ni/$NiFe_2O_4$ nanoparticles. However, using carbonaceous structures for long-term applications in OER will result in instability [16,17]. The susceptibility of carbon-based materials to oxidation under harsh reaction conditions, particularly at high operating potentials, leads to degradation and reduced performance over time, making them unsuitable for sustained use in OER applications.

Another option to generate hierarchically structured building blocks is to use supraparticles. Supraparticles are structured agglomerates, characterized by meso- and macropores and large transport channels [18], that can be generated by a scalable, one-step spray drying process. In applications such as water purification [19] and lithium-ion batteries [20], supraparticles have proven their ability to retain the advantageous intrinsic properties of individual nanoparticles and at the same time exhibit enhanced functionality through synergistic effects. This results in a singificantly improved performance than the sum of their individual components [21]. Thus, it is a valid hypothesis that the hierarchical architecture of the supraparticles can enhance accessibility of reactants to electroactive sites, facilitate ion diffusion, and improve electron transport due to enhanced interparticle connectivity and contact area [22]. Furthermore, the unique design of supraparticles is expected to contribute to the mechanical stability of the electrode, as demonstrated in lithium-ion battery applications [23], making supraparticles a promising material for durable and high-performance electrocatalytic applications. However, to the best of our knowledge, supraparticles have not yet been explored as catalyst for electrocatalytic applications like the OER.

Moreover, particle-based electrodes typically require binders like Sustainion® to improve electrode durability. As we recently demonstrated with LSCO-NP and $NiFe_2O_4$, a hydroxyl ion-conductive binder can significantly enhance the performance in the oxygen evolution reaction in half- and full cells [24]. However, as also pointed out by us [25,26] and others [27], adding a binder during ink formulation to coat the electrodes requires high-energy mixing

techniques such as sonication or ball milling. Also binder-particle interactions need to be carefully considered to ensure reproducibility. To overcome this challenge, we hypothesize that supraparticles enable to innovate an alternate strategy: by incorporating the binder (fluorine-free Sustainion®) during spray drying, it can be directly integrated into the hierarchical supraparticle architecture. This innovative method would eliminate the need for adding an additional binder during catalyst ink preparation, thereby significantly simplifying the dispersion process and at the same time enhancing the catalyst-binder interaction.

Our recent work and literature reports on $La_{0.8}Sr_{0.2}CoO_3$ perovskite nanoparticles (LSCO-NP) [24,28,29] have proven them to be potent OER electrocatalysts. Therefore, materials-wise, we selected LSCO-NP as an anode material to experimentally validate our hypothesis that the hierarchical architecture of supraparticles can enhance ion diffusion, electron transport, and accessibility to electroactive sites in electrocatalytic applications. The primary aim of this study is to demonstrate that it is possible to enhance the efficiency and scalability of OER catalysts by employing supraparticles, exemplarily using a straightforward spray drying approach to generate LSCO-SP from the respective nanoparticles. The OER performance of anodes made from LSCO-SP is systematically evaluated and compared to anodes built from their nanoparticulate counterparts. By analyzing the pore network for both approaches, we explore the role of the particle-induced microstructure of the anode in improving catalytic activity and stability. Our findings highlight the huge potential of supraparticles as a novel class of materials for the alkaline OER, enabling highly efficient and durable anodes. This study further evidences the significant role of microstructure and pore network on OER, including bubble removal and mechanical stability, and why it is important to understand the interplay of intrinsic catalytic performance and extrinsic microstructure and pore network in the anode.

2 Material and methods

2.1 Materials

The precursors used for nanoparticle formation were metal acetates: $La(CH_3CO_2)_3 \cdot 1.5H_2O$ (99.9 %, Alfa Aesar), $Sr(CH_3CO_2)_2$ (Sigma-Aldrich), and $Co(CH_3CO_2)_2 \cdot 6H_2O$ (Supelco; EMSURE® ACS grade). The solvents used in the nanoparticle synthesis included 2-ethylhexanoic acid (99 %), absolute ethanol, and acetic anhydride (≥99 %), and were all obtained from Sigma-Aldrich. Sustainion® XA-9, used as a binder for the preparation of supraparticles and electrode formation, was purchased from Dioxide Materials.

2.2 Preparation of LSCO nanoparticles via spray-flame method

The LSCO-NP were synthesized using a self-developed spray-flame reactor equipped with the standardized SpraySyn nozzle, which was developed in a previous study [24,30]. To prepare the precursor solution, stoichiometric quantities of $La(CH_3CO_2)_3 \cdot 1.5H_2O$ $Sr(CH_3CO_2)_2$, and $Co(CH_3CO_2)_2 \cdot 6H_2O$ with respect to the desired composition of the $La_{0.8}Sr_{0.2}CoO_3$ catalyst were dissolved in a solvent mixture of 35 vol% ethanol and 65 vol% 2-ethylhexanoic acid, achieving a total metal-ion concentration of 0.25 mol L^{-1}. The solution was then delivered to the SpraySyn nozzle, located at the bottom of a closed reactor chamber, at a constant flow rate of 3 mL min^{-1} using a syringe pump. Atomization of the solution was achieved using a dispersion gas mixture of O_2 (8 slm) and CH_4 (2 slm), forming a fine spray. A premixed pilot flame of methane and oxygen (2 slm CH_4/16 slm O_2) stabilized on a coaxial bronze plate was used to ignite and support the spray flame. Stable flow conditions within the reactor were maintained with a coaxial sheath gas flow of compressed air (140 slm), while the combustion chamber pressure was held at approximately 950 mbar. To cool down the particle laden reactor exhaust gas and avoid water condensation, a quenching gas flow of compressed air (230 slm) was introduced downstream of the reaction zone. The particles were deposited on a membrane filter and collected from it without further treatment for the subsequent steps.

2.3 Preparation of LSCO supraparticles via non-reactive spray drying

The LSCO-SP materials were prepared following the procedure described in our previous study [19]. A total of 0.9 g of LSCO-NP was dispersed in 300 mL of water and sonicated for 3 min using a Bandelin Sonopuls HD 2200.2 (set at 30 % amplitude). After sonication, 4.5 mL of Sustainion® (5 wt%) in ethanol was added to the catalyst dispersion, and the resulting formulation was further sonicated for an additional 2 min in an ice bath. The prepared dispersion was then fed into a laboratory-scale spray dryer (BÜCHI Labortechnik GmbH) at a rate of 5 mL/min, using nitrogen as the dispersion gas. The drying gas flow was maintained at 35 m^3/h of nitrogen, and the drying temperature was set to 150 °C. After separation by an integrated cyclone, the resulting supraparticles were collected as coarse fraction with a mass yield of approximately 70 %. The remaining 30 %, that were still in the form of nanoparticles or too-small agglomerates ended in the fine fraction and were not used in this study.

2.3.1 Fabrication of catalyst thin-film electrodes

Thin films of the active materials were applied onto nickel plates (99.2 % purity, HMW Hauner) using an airbrush coater. Before coating, the plates were treated with 1 M HCl and then rinsed with deionized water. For the LSCO-NP electrode preparation, 30 mg of LSCO-NP was dispersed in 3 mL of a 50/50 water-ethanol mixture and sonicated for 3 min at 20 % amplitude (Bandelin Sonopuls HD 2200.2). Then, 150 µL of 5 wt% Sustainion® in ethanol was added which corresponds to the Sustainion® concentration during supraparticle formation, and the dispersion was sonicated again for 3 min in an ice bath. The resulting ink was sprayed onto a nickel plate heated to approximately 100 °C. The final catalyst mass loading on the anode was 620 µg cm^{-2}.

For the LSCO-SP electrode, 30 mg of LSCO-SP was stirred in the same 50/50 water-ethanol mixture (3 mL) at 1000 rpm for 5 min without additional binder. Then, as the prepared ink was stable against agglomeration, it was sprayed onto a heated nickel plate under the same conditions as for the nanoparticles. The final catalyst mass loading on the anode was 600-650 µg cm^{-2}.

2.4 Characterization methods

2.4.1 Structural characterization of catalyst materials

X-ray diffraction (XRD) patterns of the materials were recorded in the 2θ range from 10° to 80° using a PANalytical X'Pert diffractometer, which utilized Cu K_α radiation (λ = 1.5406 Å) for the measurements. The morphology and elemental distribution of cations were observed using a JEOL JEM 2200FS transmission electron microscope (TEM) and Philips SEM XL30 scanning electron microscopy (SEM) equipped with energy-dispersive X-ray spectroscopy (EDX) for elemental mapping. Nitrogen adsorption measurements were performed to evaluate both the specific surface area and the pore size distribution using a Quantachrome Nova2000 analyzer. The specific surface area was calculated following the Brunauer-Emmett-Teller (BET) method, while the pore size distribution was derived from the adsorption-desorption isotherms using the Barrett-Joyner-Halenda (BJH) model. The hydrodynamic size (by volume) and zeta-potential of as-prepared nanoparticles and supraparticles after spray drying, both dispersed in aqueous solution, were determined by a Zetasizer Nano ZS (Malvern Instruments). The functional groups of the LSCO-NP and LSCO-SP samples were analyzed in the 400–

4000 cm^{-1} region with attenuated total reflectance Fourier transform infrared spectroscopy (ATR-FTIR, Bruker Vertex 80 spectrometer).

The pore size distribution of LSCO-NP and LSCO-SP electrodes was determined using a mercury intrusion porosimeter (PoreMaster-60, Anton Paar). The stability of the nanoparticle dispersions over time was evaluated using an analytical centrifuge (LUMiSizer LS 651, LUM GmbH). A 1 wt/v% catalyst dispersion was prepared by sonicating the powder in Milli Q (MQ) water (with a resistivity of 18.2 MΩ cm) for 3 min, followed by immediate transfer into centrifuge cells. These cells were placed in a rotor and subjected to 58 g (200 rpm) centrifugal acceleration for 20 hours. The resulting raw transmittance data were plotted as transmittograms, and interpreted according to the method outlined by Bapat et al. [31].

2.4.2 Characterization of catalyst thin-film electrodes

The morphology of the fabricated thin film electrodes was characterized using SEM (SIRION-100; FEI Co. Ltd.) at acceleration voltages of 5 and 25 kV. Surface roughness was measured using Atomic Force Microscopy (AFM, Tosca 400; Anton Paar) in contact mode with an ARROW-CONTR-20 tip (NanoWorld). The topography and roughness data obtained from the AFM measurements were analyzed using Tosca Analysis 7.4 software. Additionally, the structural changes of the catalyst material before and after the OER performance evaluation were investigated using X-ray Photoelectron Spectroscopy (XPS, Versa Probe II, ULVAC-PHI). The spectra were calibrated to the C1s peak of adventitious carbon (C–C) at a binding energy of 284.8 eV. Electron paramagnetic resonance (EPR) spectroscopy was employed to analyze the oxygen vacancies (O_{vac}) in the LSCO-NP and LSCO-SP electrodes at room temperature. The EPR spectra were recorded using an X-band Bruker Elexsys E500 spectrometer, equipped with an ESR 900 He cryostat and an ER4116DM dual-mode resonator for continuous-wave measurements. The experimental conditions included a microwave power of 10 mW, a modulation amplitude of 0.1 mT, a 600 mT magnetic field sweep centered at 325 mT, a sweep time of 60 seconds, and a microwave frequency of 9.467 GHz.

2.4.3 Electrochemistry

Electrochemical measurements were performed using a glass electrochemical beaker cell (100 mL). In the three-electrode setup, the nickel electrode with the LSCO catalyst coating acted as a working electrode, while platinum mesh was used as a counter electrode. All experiments were conducted at room temperature in purified 1 M KOH (Thermo Fisher

Scientific) electrolyte prepared using MQ water with a resistivity of 18.2 MΩ cm. Metal cations were removed using a Chelex®100 cation-exchange chelating resin (Sigma Aldrich). All potential values measured in this study were recalculated to the reversible hydrogen electrode (RHE) scale using Equation (1) [32]:

$$E_{iR}(\mathrm{RHE}) = E_{Hg/HgO} + E^{0}_{Hg/HgO} + 0.059 \cdot \mathrm{pH} - iR_u \quad (1)$$

Where E_{iR} (RHE) is the electrode potential compensated for the iR-drop in the RHE scale (V vs. RHE), $E_{Hg/HgO}$ is the measured potential versus Hg/HgO (1M KOH), and $E^{0}_{\mathrm{Hg/HgO}}$ is the standard potential of the Hg/HgO (1M KOH) reference electrode (0.098 V vs. RHE). The potentials were 100 % manually iR_u-corrected using the uncompensated resistance (R_u, **Ω**), calculated by electrochemical impedance spectroscopy (EIS) in the high-frequency range. Impedance spectroscopy measurements were obtained between 1 Mhz and 10 mHz, at working conditions of 1.6 V vs. RHE. Electrochemical data and EIS spectra were collected using a computer-controlled SP-300 potentiostat (BioLogic). The open circuit potential (OCP) was initially recorded for 60 s. Afterward, 50 cyclic voltammograms (CV) were recorded with a scan rate of 100 mV s^{-1} in a potential range of 0.0 V to 1.40 V vs. RHE. Subsequently, EIS at OCP was performed from 100 kHz to 10 Hz at 10 steps dec^{-1} to obtain the uncompensated resistance for iR_u-drop correction. Linear sweep voltammetry (LSV) was measured from 0.0 V to 1.8 V vs. RHE at a scan rate of 5 mV s^{-1}. Before the chronopotentiometry (CP) measurement for 1 h at a current density of 10 mA cm^{-2}, additional EIS at OCP was conducted in the range from 100 kHz to 10 Hz at 10 steps dec^{-1}.

3 Results and Discussion

3.1 Structural characterization of powders

The crystalline phase and structural characteristics of LSCO-NP and LSCO-SP samples were analyzed using XRD measurements, as illustrated in Figure 1. The diffraction pattern of LSCO-NP indicates a single-phase composition corresponding to the hexagonal oxygen-deficient perovskite structure of $La_{0.8}Sr_{0.2}CoO_{3-d}$. These results align well with the Bragg reflections of the reference $LaCoO_{2.937}$ perovskite structure (ICSD 153995). Importantly, in the case of LSCO-SP, XRD analysis shows that the addition of Sustainion® to the spray drying mixture did not induce any structural transformation in the perovskite phase. Furthermore, no significant differences in crystallinity were observed between LSCO-SP (9.8 nm) and

individual LSCO-NP (9.3 nm), as determined by Rietveld refinement of the XRD patterns (see supplementary material, Figure S1).

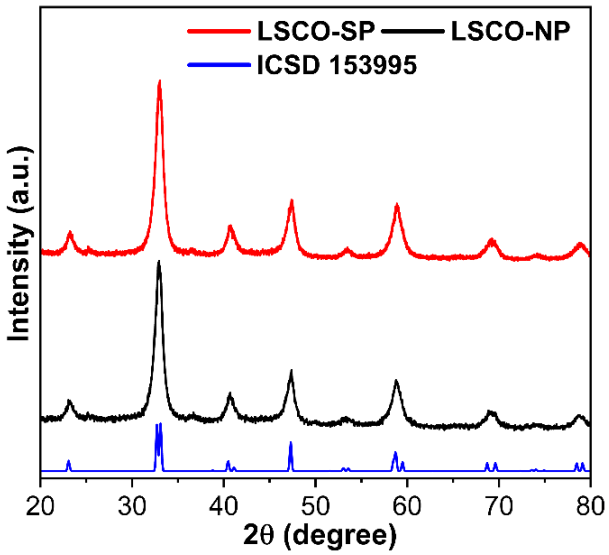

Figure 1: a) XRD patterns for LSCO-NP (black line) and LSCO-SP powders (red line).

To assess the particle size and morphology of LSCO-NP and LSCO-SP, TEM and SEM measurements were performed as shown in Figure 2. LSCO-NP exhibit a quasi-spherical shape with an average primary particle size of 8.2 nm (Figure 2a-b). There is almost no change in shape before and after the spray drying process; however, a slightly increased degree of agglomeration is observed, resulting in an average size of 10.4 nm (Figure 2e). While TEM imaging of LSCO-NP reveals individual, partly sintered crystallites, SEM shows that LSCO-NP tend to agglomerate due to van der Waals forces, particularly when analyzed in the form of the dry powder how it is obtained after spray-flame synthesis and not dispersed, as seen in the SEM image in Figure 2c.

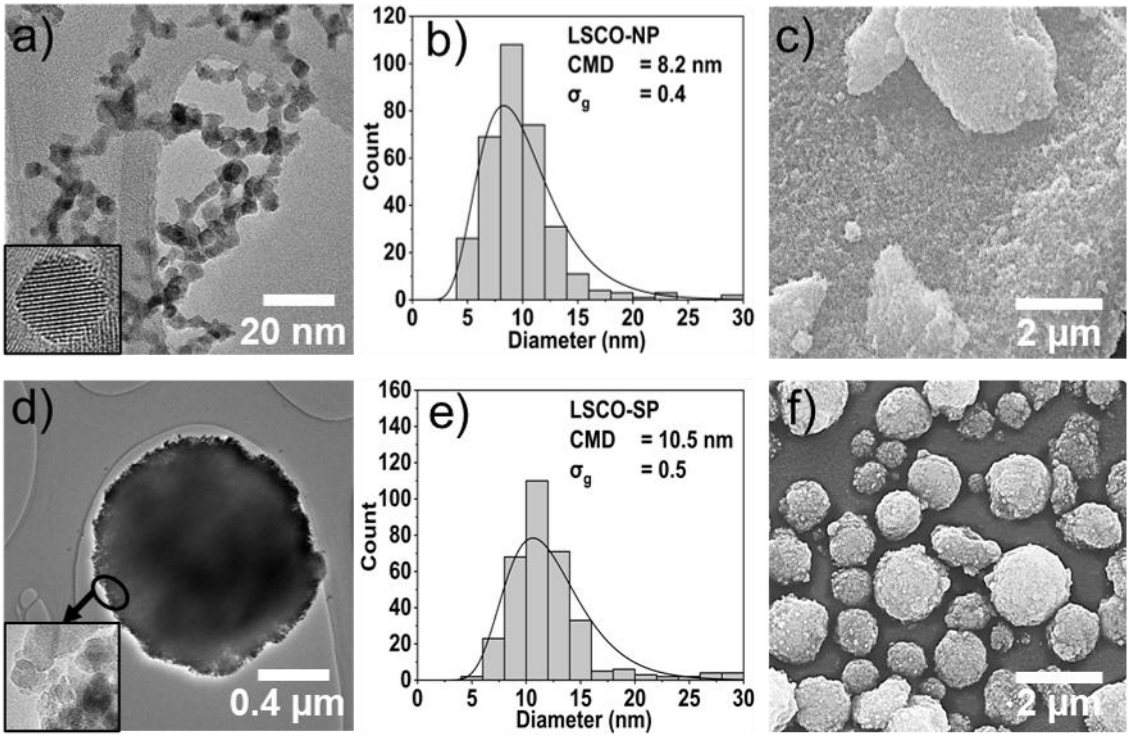

Figure 2: TEM (left) and SEM (right) images of a-c) LSCO-NP and d-f) LSCO-SP reveal differences in particle size and morphology. The count median diameter (CMD) and geometric standard deviation (σ_g) were determined by fitting the size distribution histograms of about 300 nanoparticles to a lognormal distribution.

At this point it is important to recap that for the LSCO-SP sample, Sustainion® was added to the feed for spray drying for two reasons: First, it acts as a binder, effectively holding LSCO-NP together throughout the spray drying process. This cohesive property ensures that the resulting supraparticles maintain their structural integrity, forming stable, well-defined assemblies rather than disintegrating into individual nanoparticles upon their exposure to external stress during ink formulation, coating, and OER testing. Supporting this, DLS measurements show that the average hydrodynamic size (x_{hyd}) of LSCO-SP is significantly larger than that of LSCO-NP (Figure 3a-b). Additionally, consistent with SEM data, LSCO-SP display a monomodal and relatively narrow size distribution with a volume-based relative standard deviation (RSD) of 1.6 % [33], indicating minimal size variation across the sample. The LSCO-SP also demonstrate exceptional mechanical stability, remaining intact even after extended sonication (30 min), as no significant change in the x_{hyd} was observed (supplementary material, Figure S2). Second, in line with our expectations, Sustainion® modifies the ζ-potential of LSCO-NP, shifting it from −18 to +27 mV in aqueous dispersion. Thus, it becomes clear that Sustainion® specifically interacts with the nanoparticle surface which is important out of two reasons. First, it enables the integration of the binder into the supraparticle architecture. Second, it ensures that the feed dispersion entering the spray dryer is electrostatically stabilized

against agglomeration. The high order of magnitude of the ζ-potential also ensures a homogeneous dispersion of the nanoparticles within the shrinking droplets in the spray (after the nozzle). This is important to prevent segregation and shell formation inside the droplet during drying, phenomena that typically end up in a buckled or curved supraparticle shape [21]. Therefore, in our case, dense, spherical supraparticles could be formed as a result of uniform drying rates across the droplet surface. This is confirmed by TEM and SEM images (Figure 2d-f), which evidence the presence of well-formed, spherical LSCO-SP in the final product. Additionally, the isoelectric point (IEP) changed from 5.1 for LSCO-NP to 7.4 for LSCO-SP (Figure 3c), indicating successful surface modification during the spray drying process. These findings are further supported by FTIR analysis (see supplementary material, Figure S3), confirming the adsorption of Sustainion® onto LSCO-SP®. Taken together, we expect that Sustainion® will enhance electrode durability by improving the ion exchange capacity in highly alkaline media (ca. 0.9–1.2 mmequiv g^{-1}) and at the same time enhance the mechanical stability under electrochemical conditions, while maintaining a comparable OER activity [24].

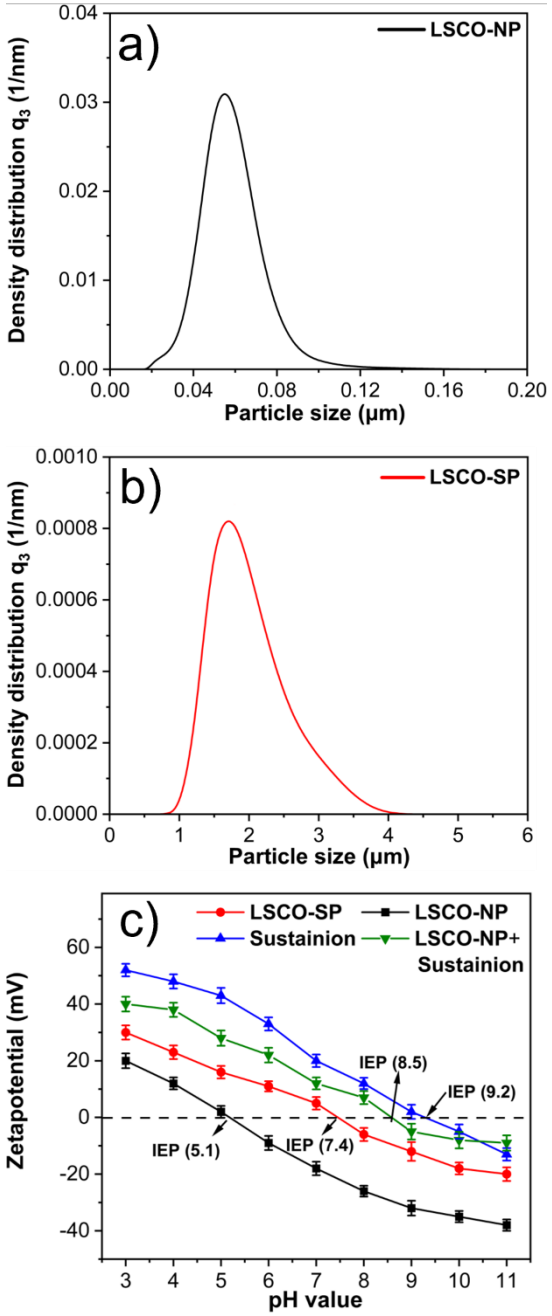

Figure 3: Particle size distributions measured via DLS of a) LSCO-NP (black squares) and b) LSCO-SP (red circles). c) The isoelectric point (IEP) shifts from 5.1 for LSCO-NP to 7.4 for LSCO-SP, indicating successful surface modification during the spray drying process.

Finally, the specific surface area of the LSCO-NP and LSCO-SP powders, determined by N_2 sorption and analyzed using BET [34], was measured as 110 $m^2\ g^{-1}$ for LSCO-NP and 72 $m^2\ g^{-1}$ for LSCO-SP. The decrease in the specific surface area observed for LSCO-SP compared to LSCO-NP is expected and can be attributed to the agglomeration of individual LSCO-NP into larger, cohesive supraparticles, leading to the partial internalization of nanoparticle surfaces and the formation of denser structures. Moreover, in line with the SEM measurements that predominantly indicate the formation of porous supraparticles (pointer to the enlargement in

Figure 2d), the measured isotherms of LSCO-SP (see supplementary material, Figure S4) showed a typical IV class according to the IU classification of adsorption isotherms [35], demonstrating the presence of mesoporous channels in LSCO-SP samples with an average pore size of 9 nm. In contrast, LSCO-NP exhibited no measurable porosity.

Taken together, the formation of a porous structure in LSCO-SP introduces a distinct internal pore network, resulting in a surface morphology that differs from that of LSCO-NP. Although the overall surface area of LSCO-SP is lower due to nanoparticle agglomeration, we hypothesize at this point and discuss in more detail later, that the mesoporous channels within the supraparticles after coating on the substrate are very important as they provide alternative pathways for reactant access and product diffusion.

3.2 Ink formulation, electrode microstructure, and property assessment

3.2.1 Ink formulation and dispersion stability

The formulation of the ink must carefully consider the physical and chemical properties of the catalysts to achieve stable and homogeneous dispersions while using cost-effective solvents and binders. Stability against agglomeration is crucial for the preparation of electrodes, which in turn affects OER activation. Therefore, it is important to understand the dispersion stability of LSCO-NP and LSCO-SP materials. Based on previous studies, a water/ethanol solvent mixture (50 vol%:50 vol%) was selected as a continuous phase, as it is known to enable LSCO-NP catalyst inks with high sedimentation stability. This mixture promotes both good adhesion between the anode catalyst layer and substrate, as well as particle-particle cohesion within the anode layer during the drying process [24]. To assess the differences between dispersions made of LSCO-NP and LSCO-SP, their sedimentation behavior was measured using transmittograms [31].

As shown in Figure 4, both catalysts, LCSO-NP (Figure 4a) and LSCO-SP (Figure 4b) dispersed well in the water/ethanol solvent mixture. However, during AC measurements, LSCO-SP exhibited faster sedimentation compared to LSCO-NP, likely due to their larger size. Additionally, the dispersion stability of the LSCO-NP and LSCO-SP inks was evaluated in the presence of fluorine-free Sustainion®® using transmittograms. At this point, it should be noted that electrode coating was only realized for LSCO-NP with binder added during ink formulation, while LSCO-SP had the binder added during spray drying. LSCO-SP without binder in the feed for spray drying exhibit a too-low mechanical stability to withstand shear

forces during dispersion, while further adding Sustainion® during the ink formulation of supraparticles is not an option out of two reasons. First, additional binders added to LCSO-SP during ink formulation would distort the comparison of their electrodes with electrodes made from LSCO-NP, because the absolute binder concentration would be altered significantly. Second, LSCO-SP become unstable upon the addition of binder, clogging the nozzle of the spray coater. However, at the level of ink formulations, all four possible permutations of powders in the solvent mixture with and without the addition of Sustainion® can be analyzed and help understand the stabilization mechanism of LSCO-SP.

As can be seen from Figure 4, the LSCO-NP remained well-dispersed with Sustainion® (Figure 4c), whereas the dispersion stability of LSCO-SP decreased significantly when LSCO-SP were mixed with the binder (Figure 4d). We relate this to a reduction in the electrostatic stabilization of LSCO-SP: Before adding Sustainion®, in the water/ethanol solvent mixture (50 vol%:50 vol%), the LSCO-SP exhibited a ζ-potential of +23 mV at pH ~5 which was sufficient to maintain good dispersion by electrostatic stabilization. However, with the addition of Sustainion®, additional positive ions were introduced into the dispersion. These cations compress the electrostatic double layer surrounding the LSCO-SP, reducing the effectiveness of electrostatic repulsion between the particles. As a result, the supraparticles experience weaker repulsive forces, leading to agglomeration and a significant decrease in dispersion stability. Thus, it can be concluded that it makes sense to use Sustainion® as a binder for the preparation of LSCO-NP anodes to prevent film delamination during OER and to sterically stabilize them. However, for the LSCO-SP that are already covered by Sustainion®, the addition of further Sustainion® compresses the double layer and causes instability. Therefore, the addition of binder can be restricted to its utilization during the spray drying process to prepare LSCO-SP. We regard this however as an elegant advantage of supraparticles that eliminates the need for any additional Sustainion® dosing during ink formulation that might be critical to control in the presence of superimposed binder adsorption at the particle surface.

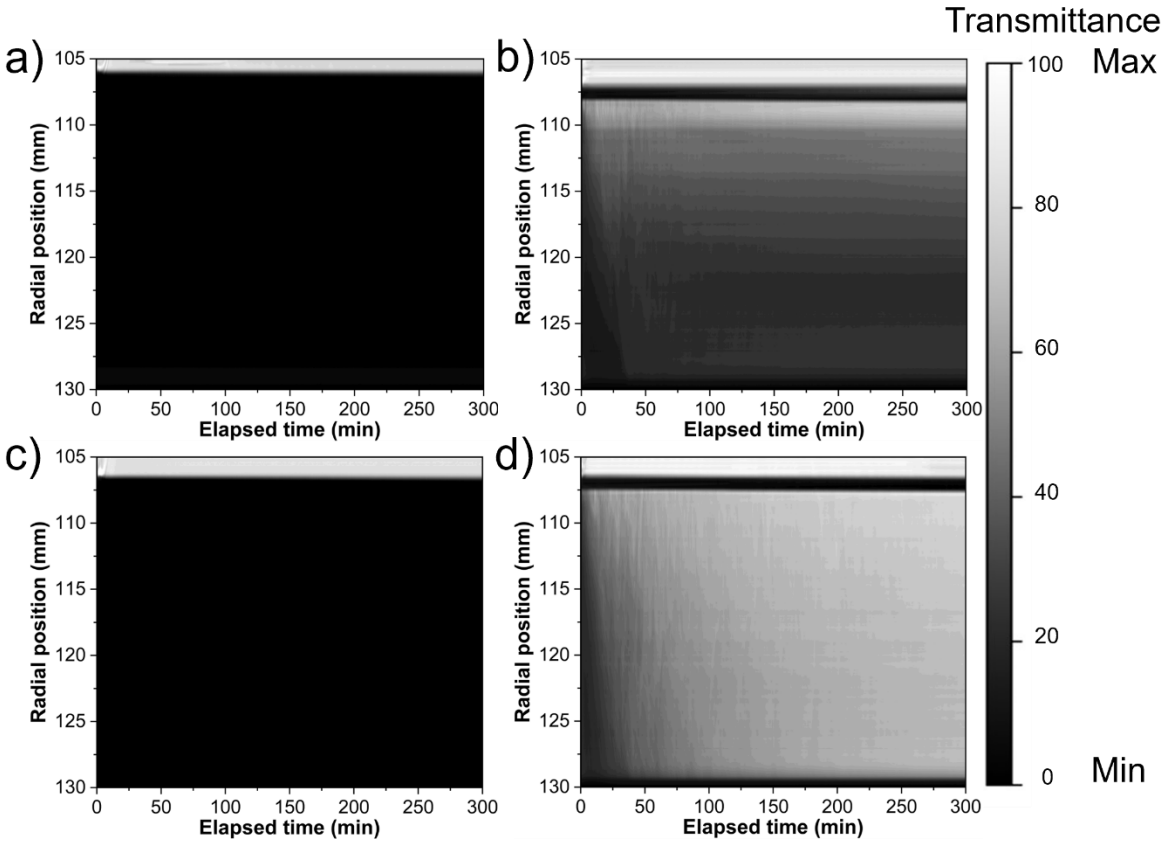

Figure 4: Stability analysis of LSCO-NP and LSCO-SP: Lower transmission (a) LSCO-NP in water/ethanol, (b) LSCO-SP in water/ethanol, and (c) LSCO-NP in water/ethanol with Sustainion® indicates fewer particles sedimenting and good stability. In contrast, higher transmission (d) LSCO-SP in water/ethanol with Sustainion® suggests low stability.

3.2.2 Characterization of catalyst thin-film electrodes: Microstructure, pore network, and anode layer properties

After ink preparation, the coating of Ni-based substrates was performed consistently using an airbrush as described in the experimental section. Electrodes were characterized using SEM, AFM, MIP, and contact angle measurements. As depicted in Figure 5a-b, the SEM images revealed that the LSCO-NP electrode exhibited a homogeneous surface with low surface roughness, while the LSCO-SP electrode surface showed the formation of large particle islands, resulting in a significantly rougher texture. Additionally, SEM/EDX elemental mapping confirmed that both LSCO-NP and LSCO-SP covered the substrate well (supplementary material, Figure S5).

To further compare the electrodes and assess their surface roughness, AFM images were recorded (Figure 5c-d). This is important as we could recently show that surface roughness, governed by the size of the building blocks and the underlying pore network, correlates with layer properties like hydrophilicity and wetting which ultimately governs bubble removal [25].

The root-mean-square roughness (S_q) values were 1200 nm for LSCO-SP and 300 nm for LSCO-NP, respectively. It is worth noting that the porous architecture of the LSCO-SP electrode not only results in a rougher surface but, more importantly, enables electrolyte penetration into the interior of the printed layer. This enhances the electrochemically active surface area and improves accessibility to active sites compared to the denser, smoother LSCO-NP electrode.

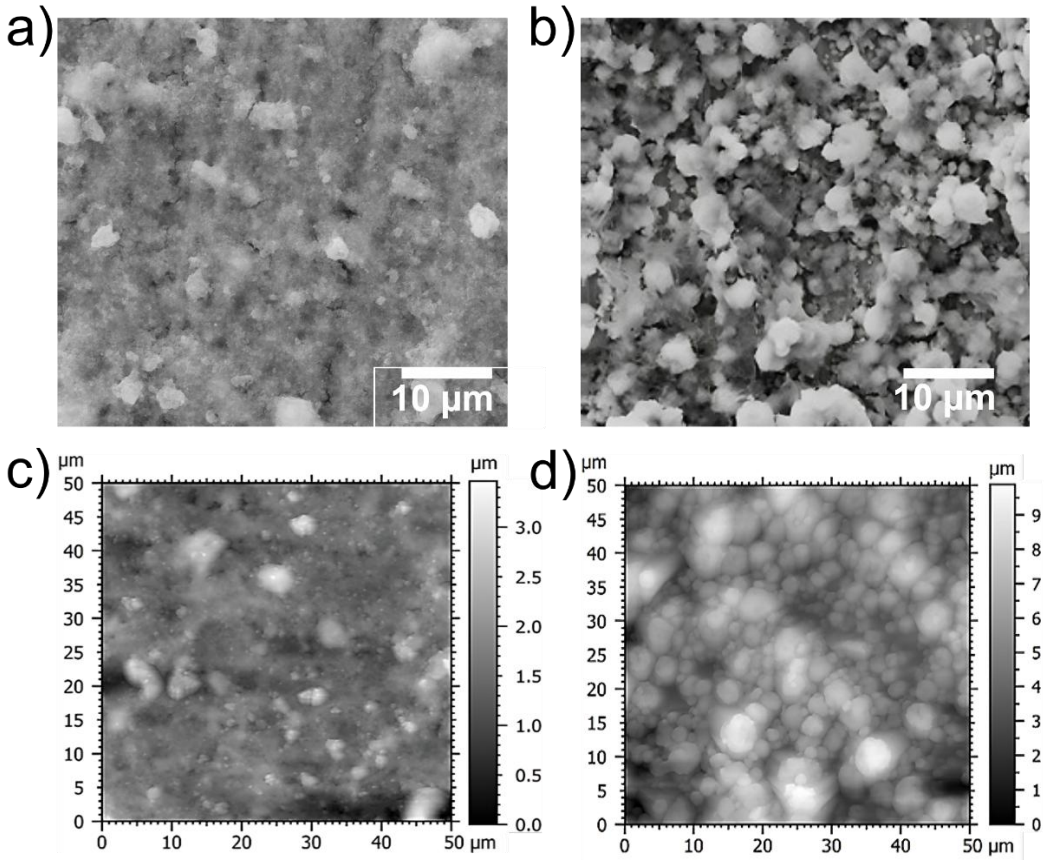

Figure 5: Surface morphology of LSCO-NP and LSCO-SP on Ni substrates. SEM images of (a) LSCO-NP and (b) LSCO-SP reveal structural differences, while AFM tapping mode topology images of (c) LSCO-NP and (d) LSCO-SP provide insights into surface texture. The S_q values were found to be 1200 nm for LSCO-SP and 300 nm for LSCO-NP, highlighting the significant increase in surface roughness for LSCO-SP.

Furthermore, cross-sectional SEM images of the coated electrodes were recorded to evaluate structural differences (Figure 6a and Figure S6). The LSCO-NP coating formed a uniform, densely packed layer on the nickel substrate with no detectable porosity, as confirmed by MIP analysis (Figure 6b). This lack of pores aligns with expectations for such ultrafine nanoparticles, resulting in a dense and compact structure. In contrast, the LSCO-SP electrode demonstrated pronounced hierarchical porosity, with an overall porosity of approximately 65 % as revealed by cross-sectional SEM analysis (Figure 6a and Figure S7). About 35 % of

the overall porosity in the electrode is intra-supraparticle, which accounts for 50 % of the porosity within the supraparticles themselves (up to 100 nm). The remaining 30 % of the porosity comes from inter-supraparticle voids and channels, extending up to 1 µm between the assembled supraparticles. This porosity was further characterized using MIP analysis, revealing a bimodal pore size distribution. Based on the IUPAC definitions, approximately 37 % of the pores were classified as mesopores, centered around 27 nm, while 63 % were macropores, distributed around 65 nm (by volume). Notably, while MIP analysis is limited to larger pores, BET measurements (Figure S4) of the LSCO-SP powder prior to coating identified the presence of small mesopores (~9 nm).

The hierarchical porosity in LSCO-SP originates from its supraparticle assembly and the multiscale porous network that exists at two distinct levels: (i) At the supraparticle level (in the powder before coating), mesopores (up to 50 nm) and macropores (up to 100 nm) are embedded within individual particles, facilitating improved access to electrochemically active sites and promoting efficient diffusion throughout the coating, and (ii) at the printed layer level, larger macropores (up to ~1 µm), observed in cross-sectional SEM images (Figure S7), enhance electrolyte penetration and transport. These mesopores integrate with the larger macropores, forming a hierarchical porous structure. This multiscale framework can enhance surface accessibility and promote improved reactant diffusion.

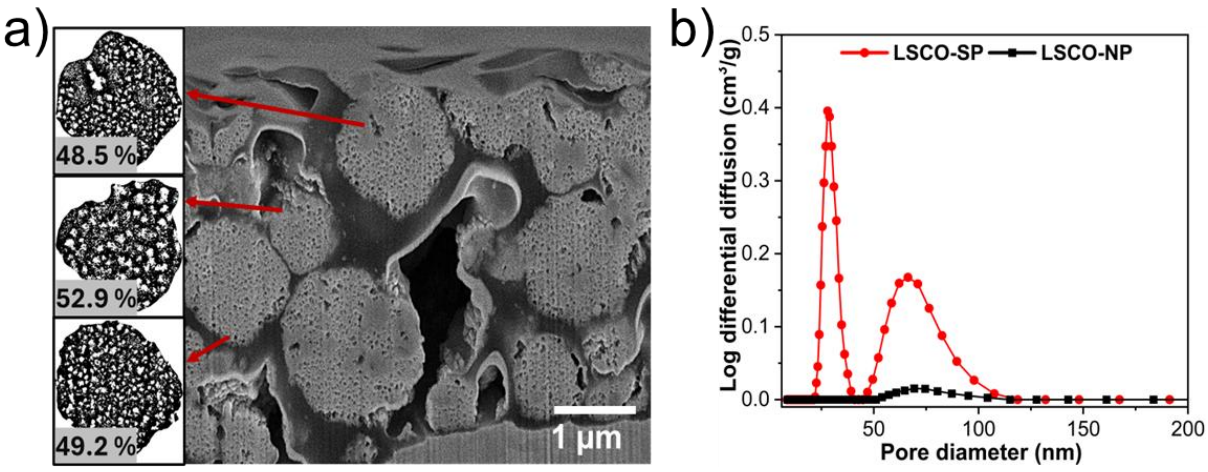

Figure 6: a) FIB-SEM cross-section of LSCO-SP electrodes, and b) pore size distribution of LSCO-SP on Ni substrates, determined by MIP analysis, highlighting the porous structure.

In addition, to assess the initial surface wettability of the anode layer, contact angle measurements were conducted with 1 M KOH for both LSCO-NP and LSCO-SP electrodes (pre-OER) to understand the interaction between the electrode surface and the electrolyte (Figure 7). The LSCO-NP electrode exhibited a contact angle of 92 ± 1 °, while the LSCO-SP

displayed a contact angle of 113 ± 2 °. Thus, both electrodes fall within the lyophobic regime (> 90 °). In our previous study, we found that for anodes with similar chemical characteristics, the microstructure and pore network significantly affect the initial electrode wetting [36]. This study also emphasizes the potential applicability of the Cassie-Baxter model for porous substrates known from surface-liquid analysis in the field of colloids and thin films. In brief, it describes a porous thin film as a heterogeneous system consisting of a solid (here the LSCO particles) and air (the pores) on top of which the droplet sits. According to the Cassie-Baxter equation, the contact angle is proportional to the air entrapment within the porous network of the catalyst layer [37]. That means the higher the porosity and surface roughness, the higher the contact angle. This perfectly aligns with our AFM and pore analysis results.

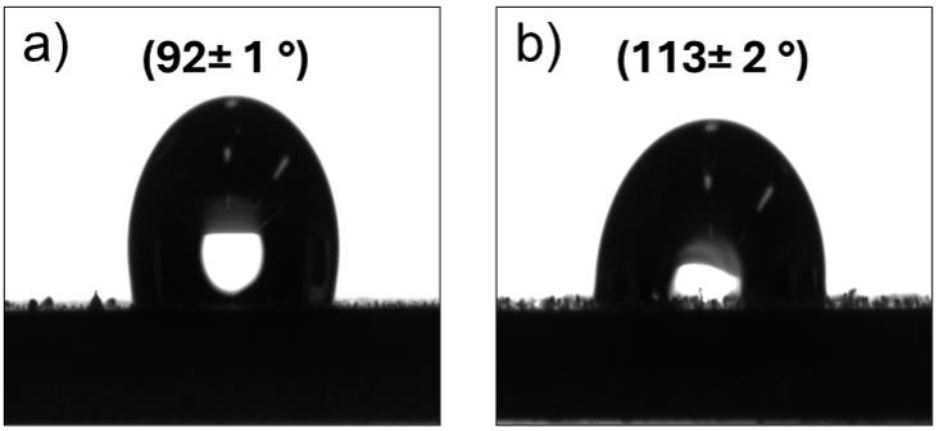

Figure 7: Contact-angle measurements of (a) LSCO-NP and (b) LSCO-SP on Ni substrates using 1 M KOH solution, revealing different wettability. Both samples fall within the lyophobic regime (>90°).

To summarize, we found that the LSCO-SP electrode has higher surface roughness, greater porosity, and increased lyophobicity compared to the LSCO-NP electrode. AFM analysis confirmed the higher surface roughness of LSCO-SP, providing more accessible active sites. Cross-sectional SEM and MIP analyses revealed a hierarchical porous structure in LSCO-SP, while contact angle measurements showed LSCO-SP to be more lyophobic. We hypothesize that the combined effects of increased surface roughness, hierarchical porosity, and higher lyophobicity of the LSCO-SP electrode will contribute to improved electrochemical performance. Specifically, these structural characteristics are expected to enhance access to active sites, promote better reactant diffusion, and facilitate more efficient bubble management, all of which are essential for high catalytic efficiency under OER conditions. The following sections will explore how these structural features influence the electrochemical behavior of the electrodes in greater detail.

3.3 OER catalytic performance evaluation

The electrocatalytic OER performance of the LSCO-NP and LSCO-SP electrodes was evaluated using a standard three-electrode system under uniformly distributed potential conditions, as described in our previous work [24]. The aim of these experiments was to systematically compare the intrinsic activity, charge transfer resistance, and bubble management capabilities of the two electrode types. These aspects are important for understanding the suitability of the materials for practical water-splitting applications.

To provide a clear framework for the discussion, the experimental results are organized into three main areas. First, the intrinsic activity of the electrodes was evaluated using LSV to determine the overpotential, with Tafel analysis used to assess the reaction kinetics. Second, the contact resistance was investigated through EIS to measure the charge transfer resistance at the electrode-electrolyte interface. Finally, bubble management was assessed via CP at current densities of 10 mA cm^{-2} and 100 mA cm^{-2} to evaluate the performance of the electrodes, the latter under conditions with significant bubble formation.

3.3.1 Intrinsic activity evaluation

According to the LSV results (Figure 8a), the LSCO-SP catalyst demonstrated enhanced OER performance, achieving a potential of 1.55±0.004 V vs. RHE at a current density of 10 mA cm^{-2}, compared to 1.57±0.001 V for the LSCO-NP electrodes. This 20 mV reduction in overpotential highlights the intrinsic activity enhancement of LSCO-SP, confirming its improved efficiency in facilitating the OER at a given current density and its ability to lower energy barriers for the reaction. Further insights into the reaction kinetics were obtained from Tafel slope analysis (Figure 8b). The LSCO-SP electrodes exhibited a Tafel slope of 76.2 mV dec^{-1}, while the LSCO-NP electrodes showed a slope of 82.5 mV dec^{-1}, indicating faster electrocatalytic kinetics of LSCO-SP electrodes. This improvement is attributed to the hierarchical porous structure of LSCO-SP, which enhances the accessibility of active sites and reduces kinetic barriers for the OER.

3.3.2 Contact resistances analysis

To evaluate the charge transfer resistance at the electrode-electrolyte interface, EIS was performed. As shown in Figure 8c, the LSCO-SP (2.48 Ω) catalyst exhibited a smaller Nyquist

semicircle diameter compared to LSCO-NP (4.93 Ω), indicating a lower charge transfer resistance at the electrode-electrolyte interface. Specifically, LSCO-SP electrodes demonstrated a charge transfer resistance of 1.11 Ω, whereas LSCO-NP electrodes exhibited 1.31 Ω. This reduction in resistance for LSCO-SP is attributed to its high interparticle connectivity, which enhances electron transport within the electrode structure. The porous architecture of the LSCO-SP electrode, as confirmed by MIP analyses (Figure 6b), plays a key role in enhancing ion transport and improving the accessibility of active sites for the reaction. Unlike the compact structure of LSCO-NP, the LSCO-SP electrode exhibits meso- and macroporous channels (Figure 6a-b), which provide efficient pathways for ion diffusion that are crucial for the resulting OER activity.

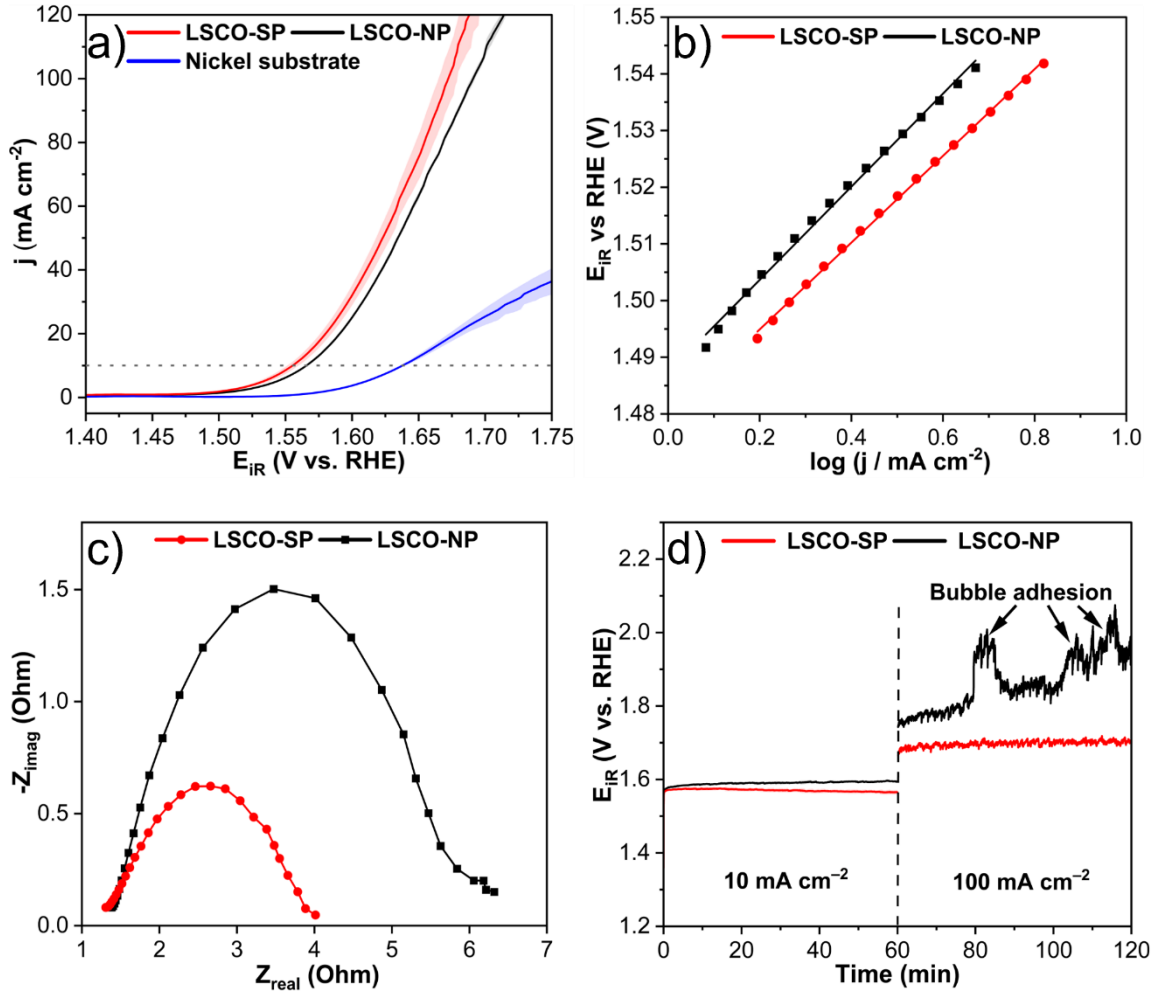

Figure 8: Electrochemical performance of LSCO-NP (black) and LSCO-SP (red) coated on Ni plates. (a) Averaged LSV polarization curves, (b) Tafel plots, (c) Nyquist plots, and (d) multistep chronopotentiometries at 10 and 100 mA cm^{-2}, measured in 1.0 M KOH with a scan rate of 5 mV s^{-1} in a beaker cell. The dashed areas represent the standard deviations.

3.3.3 Bubble management performance

Bubble formation and detachment play a critical role in determining the stability and efficiency of electrodes during OER, especially at higher current densities where bubble accumulation can hinder OER performance. Therefore, CP measurements were conducted at 10 mA cm^{-2} and 100 mA cm^{-2} (Figure 8d) to assess bubble management under operational conditions. At 10 mA cm^{-2}, the LSCO-SP electrodes demonstrated stable performance, with a slight potential decrease from 1.57 V to 1.56 V over time, while for LSCO-NP, the potential increased from 1.57 V to 1.60 V. However, at 100 mA cm^{-2}, where bubble formation becomes pronounced, the LSCO-SP electrodes maintained stable activity with a potential of 1.70 V. In contrast, the LSCO-NP electrodes experienced more significant performance degradation, with the potential reaching 2.00 V. This highlights the critical role of efficient bubble removal in OER, as the rapid accumulation of oxygen bubbles at higher current densities can obstruct reactant diffusion, reduce access to active sites, and severely impair catalytic efficiency. This behavior is particularly evident when comparing electrodes made from LSCO-SP and LSCO-NP. Contact angle measurements, as shown in Figure 7 of the previous section, reveal that electrodes made from LSCO-SP exhibit a higher lyophobicity (113°) compared to those made from LSCO-NP (92°). This increased lyophobicity facilitates the detachment of oxygen bubbles from the electrode surface by creating non-wetting areas, which form pathways for bubble movement, allowing the bubbles to grow larger and detach more easily [38]. The efficient removal of oxygen bubbles prevents their adhesion on the electrode surface, ensuring continuous access of reactants to active sites and minimizing the impact of bubble-related hindrances to catalytic activity. In contrast, LSCO-NP electrodes, with their lower lyophobicity and denser structure, suffer from bubble accumulation. This accumulation obstructs reactant diffusion, reduces active site utilization, and introduces mass transport limitations. The higher noise observed in stability measurements for electrodes made from LSCO-NP further indicates the negative effects of bubble buildup, which impedes stable catalytic performance. This issue is significant at higher current densities, where the rapid formation of bubbles obstructs mass transport, thereby severely limiting the OER efficiency.

Additionally, AFM characterization (as shown before in Figure 5c-d) of the LSCO-SP electrodes revealed significantly increased surface roughness (S_q = 1200 nm) compared to the smoother LSCO-NP electrodes (S_q = 300 nm). This higher surface roughness not only provides more accessible active sites but also aids in bubble management. The increased surface

roughness can help facilitate the detachment and movement of bubbles by providing non-wetting regions where the bubbles can more easily separate from the electrode surface [39]. The combined effects of surface roughness and hydrophobicity, emulating the 'self-cleaning' properties of lotus leaves, can enhance bubble detachment [40]. In contrast, the smoother, more compact surface of LSCO-NP electrodes promotes bubble accumulation, which obstructs access to active sites and reduces catalytic efficiency. Therefore, the combination of increased surface roughness and higher lyophobicity in LSCO-SP electrodes works synergistically to improve bubble removal, ensuring continuous access to active sites and maintaining high catalytic activity, particularly under conditions of pronounced bubble formation.

Taken together, the formation of LSCO-SP, characterized by their distinct hierarchical porous structure, their increased surface roughness, and their enhanced electron transport pathways, significantly boosts the final OER performance. These structural features improve electrode resilience under high operational currents, enabling sustained high-performance activity and long-term stability. Such way, the unique architecture of LSCO supraparticles effectively addresses the limitations of nanoparticle-based electrodes, ensuring continuous catalytic activity and efficient performance, even at elevated current densities. However, to gain further insight into the stability of the LSCO-NP and LSCO-SP electrodes, it is necessary to explore the changes in their chemical composition and morphology after one hour of electrolysis. The post-mortem characterization, including XPS and morphological analysis discussed in the next chapter, provides important insights into material degradation during the OER process. This analysis helps confirm the resilience of the electrode structures and their ability to maintain high catalytic efficiency over time, particularly under high operational currents.

3.4 Post-mortem characterization

First of all, morphological characterization of the LSCO-NP- and LSCO-SP-based electrodes after OER testing was performed to assess their structural integrity (see supplementary material, Figure S8-9). Post-OER SEM and AFM images showed that catalysts of both the LSCO-NP- and LSCO-SP-based electrodes retained their multi-layered architectures, demonstrating robust structural stability even after extended reaction cycles. This preserved morphology suggests that both catalysts, nanoparticles and supraparticles, effectively withstand the mechanical and chemical stresses induced by OER conditions, which is essential for maintaining their long-term catalytic performance.

To investigate the changes in the chemical composition of the catalytically active materials LSCO-NP and LSCO-SP during the OER, XPS spectra were recorded before and after electrolysis (

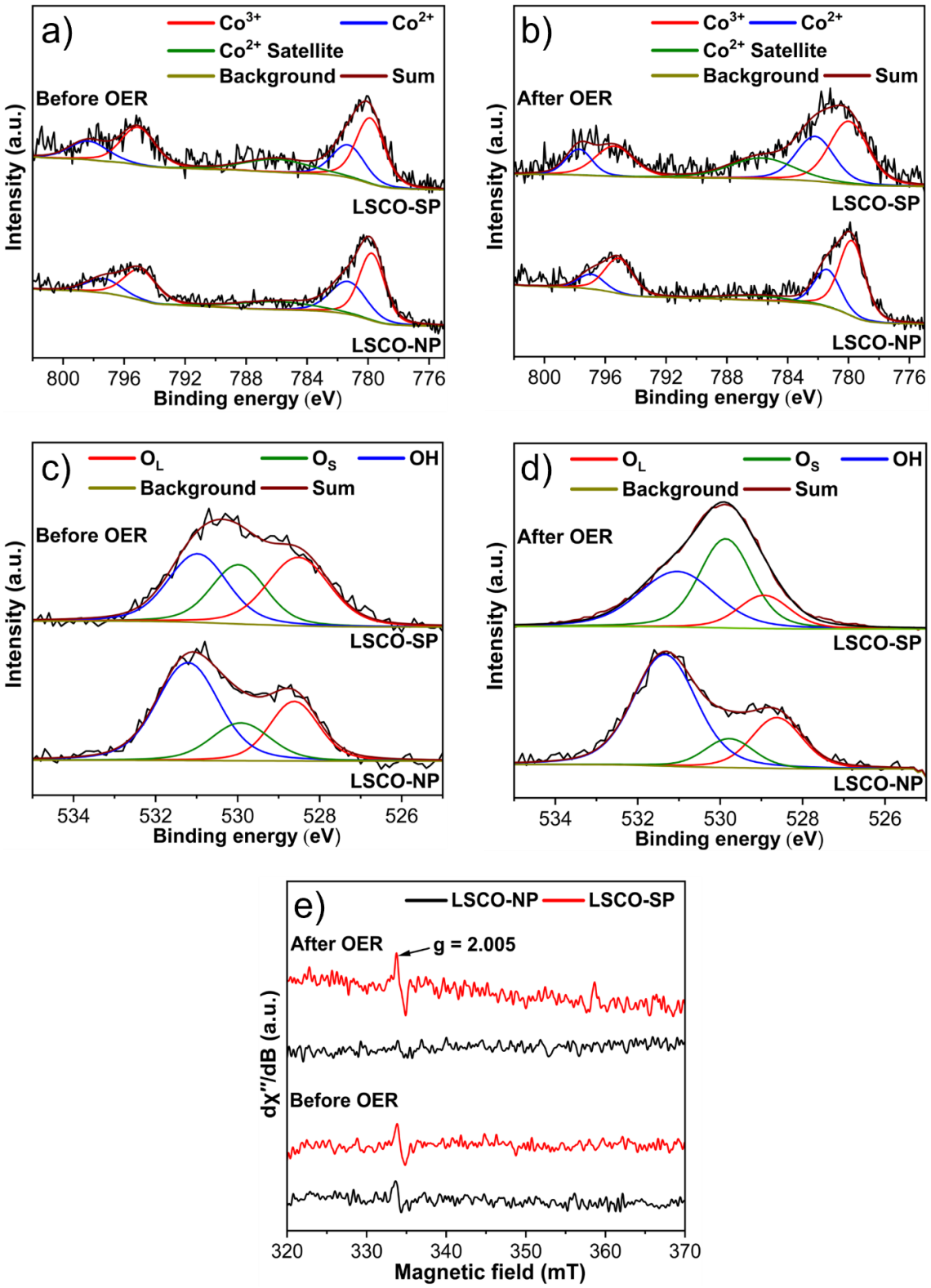

Figure 9). This analysis provides insights into the changes in the transition metal ion valence states throughout the OER process. As expected, the spectra of the La3d and Sr3d ions from electrodes made of both LSCO-NP and LSCO-SP, showed no significant changes in their chemical environment (see supplementary material, Figure S10), indicating that the perovskite structure remained stable. However, notable differences were observed in the Co2p and O1s spectra between the LSCO-NP and LSCO-SP samples. The surface Co2p XPS spectra for both types of electrodes, before electrolysis, exhibited peaks around 780 eV and 795 eV, corresponding to the $Co2p_{3/2}$ and $Co2p_{1/2}$ spin-orbit states [30]. The energy difference of the doublet (approximately 15.2–15.3 eV) is characteristic of cobalt in the perovskite environment. Both signals as well as the additional, minor satellite peaks in the $Co2p_{3/2}$ region, between 785 eV and 790 eV suggest the presence of both Co^{3+} and Co^{2+} at the catalyst surface. After electrolysis, the LSCO-SP electrode showed an increase in the intensity of the Co^{2+} peaks, especially at 782.4 eV along with the increased satellite peak intensity near 785 eV, indicating a further reduction of Co^{3+} to Co^{2+} during the OER. The O1s spectra support these findings. Therefore the O1s spectra were deconvoluted into three main peaks at 528.6 eV, 529.6 eV, and 531.4 eV, which are assigned to surface lattice oxygen (O_L), surface adsorbed oxygen species (O_s: O_2^{2-} and O^-), which are related to surface O_{vac}, and surface hydroxyl groups (OH), respectively (

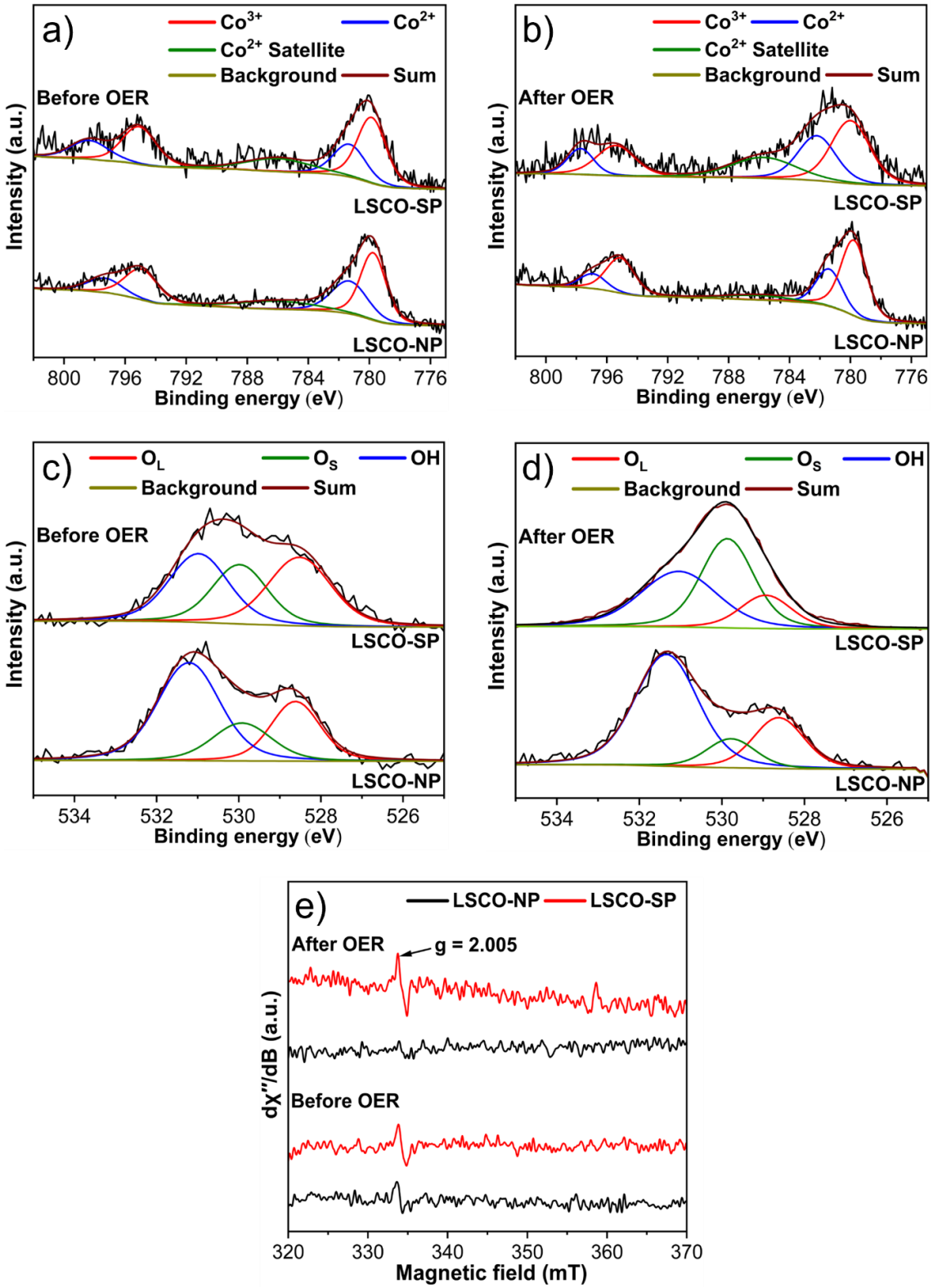

Figure 9c-d) [41]. The ratio of O_s/O_L(peak area from

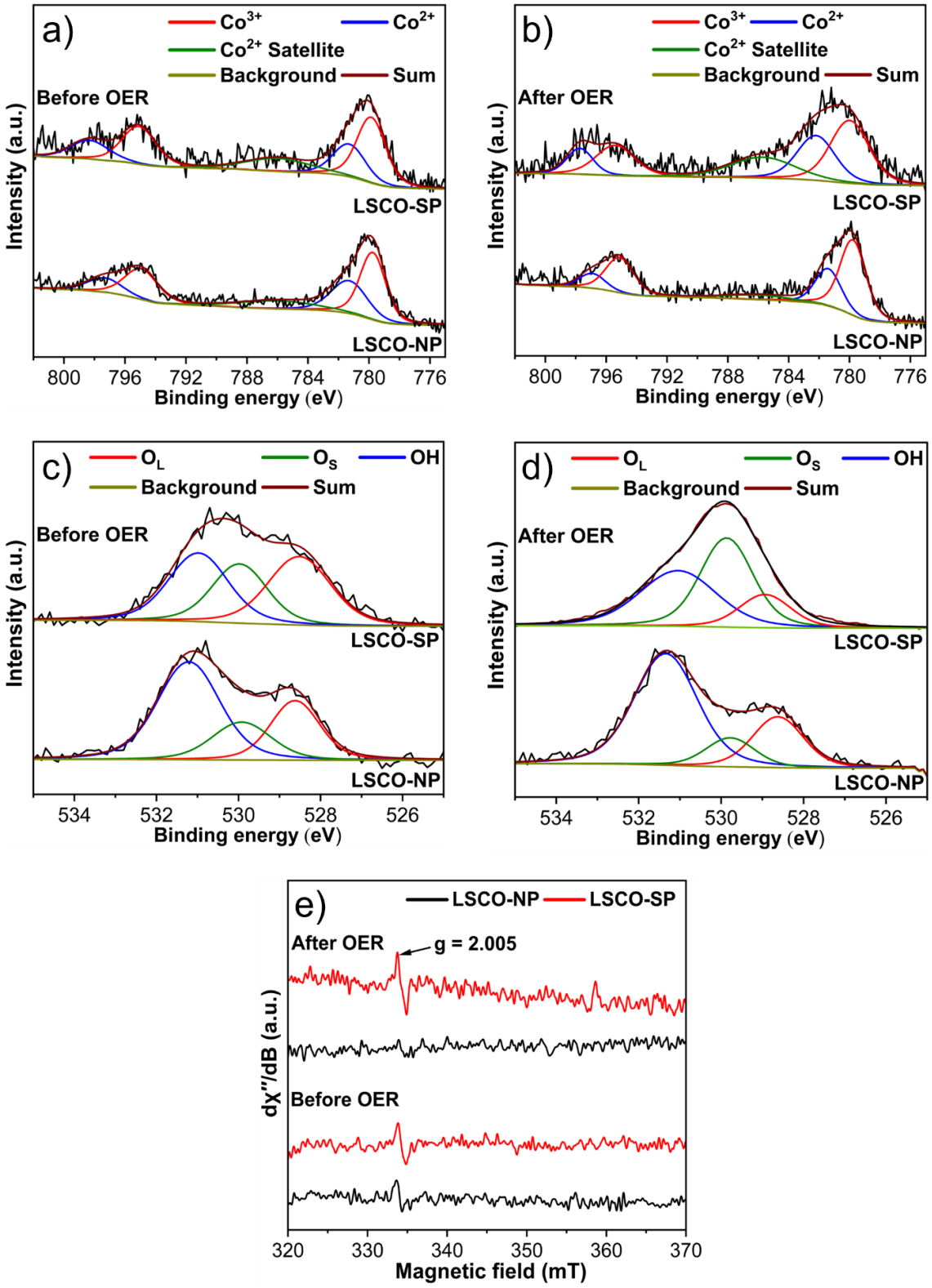

Figure 9c-d) can be used to estimate the relative concentration of surface O_{vac}, with a higher ratio corresponding to a greater concentration of O_{vac} [42–44].

Prior to electrolysis, the ratio of O_s/O_L in LSCO-SP was 0.75, which increased significantly to 2.7 after electrolysis. This increase suggests that more O_{vac} formed on the surface during the

OER process. In contrast, electrodes made of LSCO-NP exhibited an initial O_s/O_L ratio of 0.77, which decreased to 0.56 post-electrolysis. We believe this finding to be very important as it suggests that, during the OER, a part of the Co^{3+} ions in electrodes made from LSCO-SP were reduced to Co^{2+}, which facilitated the formation of O_{vac}.

To further confirm the presence of O_{vac}, EPR was applied to the LSCO-NP and LSCO-SP samples (

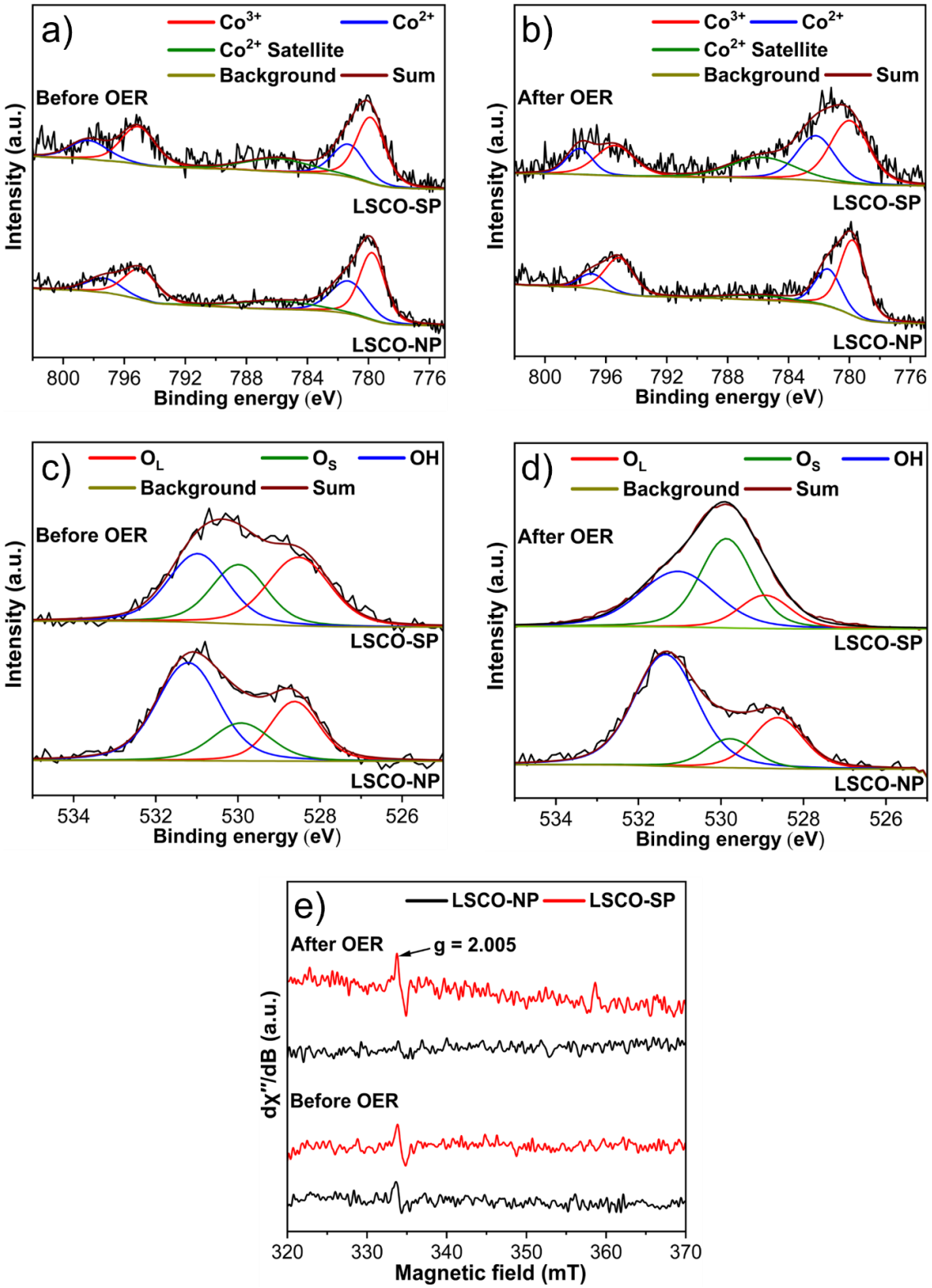

Figure 9e). The narrow signal observed at g = 2.005 corresponds to the O_{vac}. However, the signal intensity was relatively low for all samples, likely due to the presence of Sustainion® on the surface of the electrodes, which may reduce the EPR signal strength. The increased EPR signal in LSCO-SP compared to LSCO-NP after electrolysis indicates that O_{vac} plays a crucial role in

the OER mechanism. The formed O_{vac} act as active sites, enhancing OER performance by facilitating interactions with hydroxyl ions (OH^-), which is essential for efficient oxygen release [45]. The detailed mechanism of this process will be discussed in the following section. Moreover, studies on similar materials have shown that hierarchical structures, like nanosheets or nanowires on nanospheres, tend to exhibit a significantly increased O_{vac} concentration because their architecture allows for a more efficient redistribution of electronic density and accommodation of structural defects under catalytic conditions [46–48].

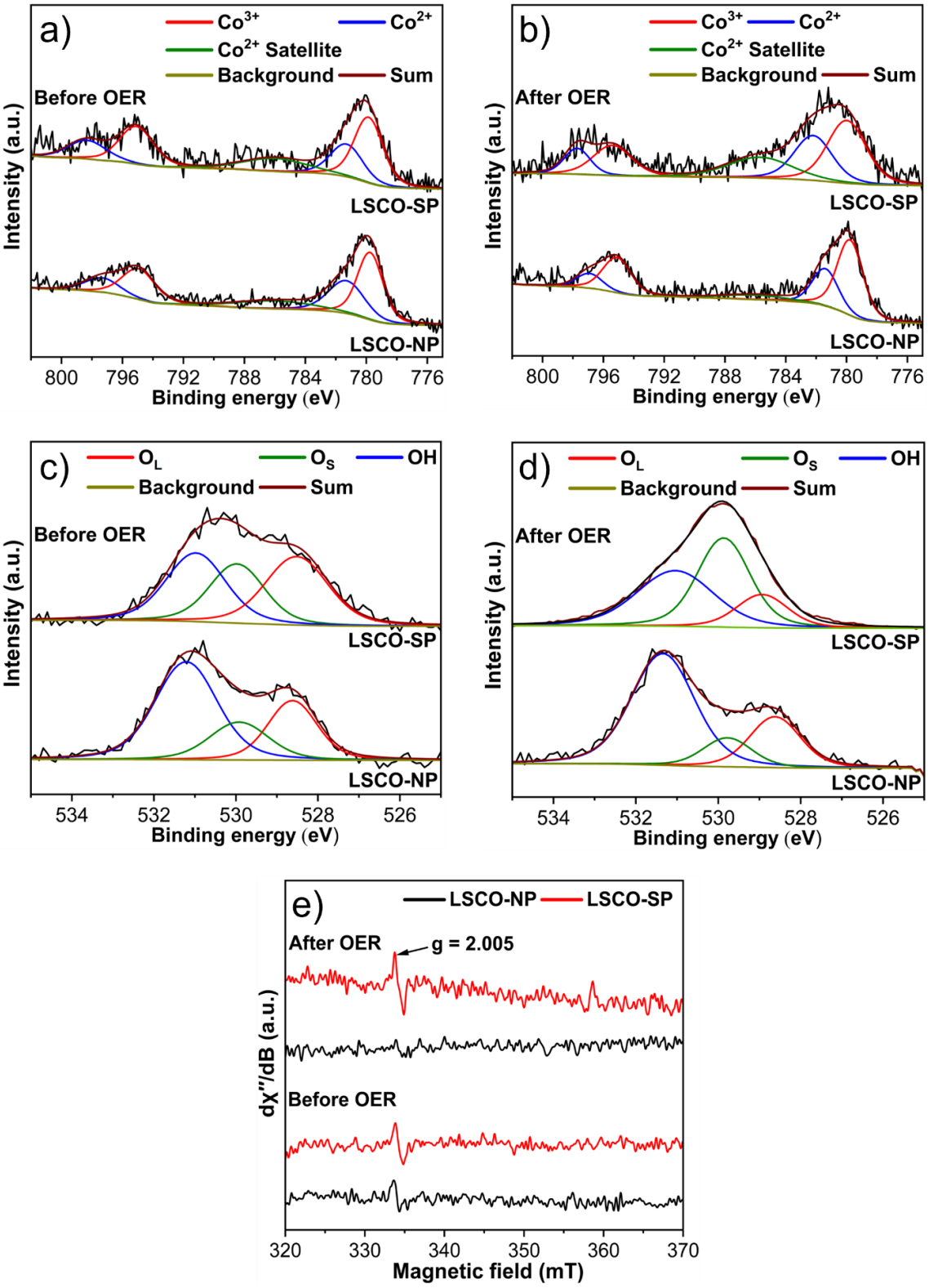

Figure 9: XPS and EPR analysis of LSCO-NP and LSCO-SP electrodes before and after electrolysis. (a-b) Co 2p and (c-d) O 1s XPS curve fits show changes in the chemical state and O_{vac} behavior of the electrodes. (e) EPR spectra plotted as $d\chi''/dB$, where χ'' denotes the absorptive part of the high-frequency susceptibility over magnetic field, reveal the presence of O_{vac}, highlighting their role before and after electrolysis.

The post-mortem characterization results reveal significant changes in the surface chemistry of the LSCO-NP and LSCO-SP electrodes during the OER, particularly with respect to the surface cobalt oxidation states and oxygen species. These findings provide important insights into the catalytic behavior of these materials under operational conditions. Building upon this, we explore the specific reaction mechanisms involved, with a particular focus on the contributions of the adsorbate evolution mechanism (AEM) and lattice oxygen oxidation mechanism (LOM) to the overall OER. The interplay between these mechanisms, as influenced by the observed surface chemical changes, is key to understanding the enhanced catalytic performance of LSCO-SP electrodes. In the following chapter, we focus on how the Co^{2+}/Co^{3+} transition and the formation of active oxygen species influence these reaction pathways.

3.5 Mechanism of OER

Perovskites in alkaline OER systems typically follow either the traditional AEM or the LOM [49]. As shown in Figure 10, the AEM mechanism is directly related to the redox activity of cobalt. Specifically, Co^{2+}/Co^{3+} and Co^{3+}/Co^{4+} transitions, occurring at 1.18 V and 1.31 V vs. RHE (Figure 10a), respectively, indicate that the Co surface in LSCO-SP undergoes partial oxidation to cobalt oxides/oxyhydroxides in the pre-OER potential region [43,50]. However, the central characteristic of LOM is the direct O–O bonding between lattice oxygen and adsorbed oxygen, which can bypass the AEM mechanism. The initial steps of the LOM involve the interaction with hydroxide ions in solution and the release of H_2O. Subsequently, O–O bonds are formed within the intermediate, followed by oxygen release, and O_{vac} generation (previously confirmed via XPS and EPR analysis) [51]. Then, O_{vac} acts like an accumulation site and promotes the adsorption of key intermediates such as OH^-, O^{2-}, and OOH^-, thereby accelerating the OER kinetics [52].

To distinguish between the contributions of AEM and LOM, it is crucial to track negatively charged oxygenated species (e.g., O_2^{2-}). Tetramethylammonium cation (TMA^+) specifically inhibits those negatively charged oxygen species that contribute to the LOM pathway [51,53]. To prove the effect of LOM, LSV measurements of LSCO-SP electrodes in 1 M KOH and 1 M TMAOH solution were carried out (see supplementary material, Figure S11). A significant increase in overpotential was observed after exposure to 1 M TMAOH, compared to 1 M KOH. This indicates a suppressed LOM mechanism, confirming its significant contribution to the overall OER process. In summary, these results suggest that the LOM plays an important role

in the enhanced OER performance of LSCO-SP electrodes, which can be tuned through strategic electrode design and fabrication.

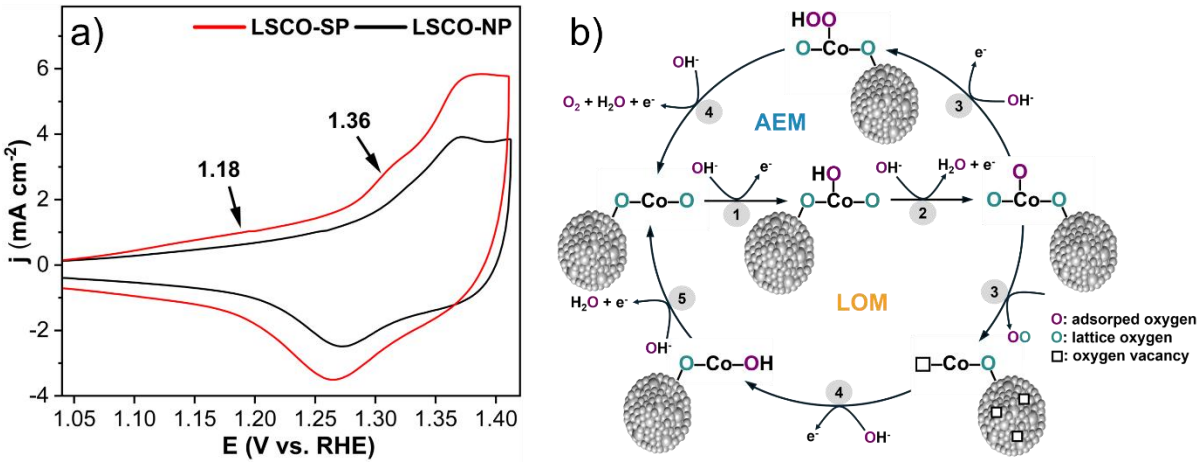

Figure 10: a) CV curve of LSCO-SP supported on Ni electrode compared with CV curves of electrodes generated by LSCO-NP coated on Ni plates and b) proposed OER mechanism of electrodes made from LSCO-SP.

4 Conclusions

In this study, we have demonstrated a scalable and effective approach to synthesize hierarchical LSCO-SP for enhancing OER performance in alkaline conditions. The superior catalytic activity and stability of LSCO-SP are attributed to the following key features:

Firstly, the hierarchical structure of the SP layers enables improved access to the reactive surface and facilitates efficient ion diffusion, which enhances the OER performance. The LSCO-SP catalyst showed an overpotential of 1.55 V at 10 mA cm^{-2}, compared to 1.57 V for the LSCO-NP, demonstrating its superior OER activity.

Secondly, the hierarchical design of LSCO-SP promotes rapid electron transport, lowering the energy barrier for oxygen evolution, as evidenced by a lower Tafel slope of 76.2 mV dec^{-1}, compared to 82.5 mV dec^{-1} for LSCO-NP, indicating faster catalytic kinetics.

Thirdly, the increased concentration of O_{vac} on the surface of LSCO-SP, as confirmed by XPS and EPR analysis, contributes to more efficient hydroxyl ion interactions and better oxygen evolution.

Fourthly, LSCO-SP demonstrate remarkable stability under high current densities, with sustained activity as shown by CP tests. At 100 mA cm^{-2}, electrodes made from LSCO-SP

maintained their catalytic performance, unlike electrodes based on LSCO-NP, which showed significant degradation under similar conditions.

Fifthly, electrodes made from LSCO-SP maintained their structural integrity and performance over extended operation cycles, offering improved durability compared to their nanoparticle-based counterparts.

Finally, electrodes based on LSCO-SP exhibit superior charge transfer properties, with a lower charge transfer resistance (1.11 Ω), compared to 1.31 Ω for LSCO-NP, further supporting their enhanced OER kinetics.

Overall, the design of LSCO-SP offers a promising and cost-effective approach for efficient and durable oxygen evolution. Their hierarchical porous structure enhances active site accessibility, ion diffusion, and electron transport, leading to superior catalytic performance and stability. The supraparticle architecture also improves bubble management and maintains a high electrocatalytic activity under elevated current densities. Finally, the innovative design of LSCO-SP facilitates scalability through roll-to-roll coating techniques, making supraparticles strong candidates for large-scale, sustainable water-splitting and renewable energy applications, noteworthily not only for alkaline water electrolysis (AEL) but also for anion exchange membrane water electrolysis (AEMWE).

Acknowledgments

This material is based upon work supported by the Mercator Research Center Ruhr (MERCUR) within the DIMENSION project. B.Toplak gratefully acknowledges a scholarship from the International Max Planck Research School (IMPRS) RECHARGE doctoral program. The authors thank Dr. M. Heidelmann and Dr. U. Hagemann from the Interdisciplinary Center for Analytics on the Nanoscale (ICAN). The X-ray data were collected using the Rigaku Smartlab High Resolution X-ray diffractometer of the Nanoparticle Processing Technology (NPPT) group at the University Duisburg-Essen. The instrument is funded through the DFG (German Research Foundation) Instrument proposal INST 20876/395-1 FUGG and the state of North Rhine-Westfalia, Germany.

5 References

[1] M. Amir, R.G. Deshmukh, H.M. Khalid, Z. Said, A. Raza, S.M. Muyeen, A.-S. Nizami, R.M. Elavarasan, R. Saidur, K. Sopian, Energy storage technologies: An integrated survey of developments, global economical/environmental effects, optimal scheduling

model, and sustainable adaption policies, J. Energy Storage. 72 (2023) 108694. https://doi.org/https://doi.org/10.1016/j.est.2023.108694.

[2] Q. Hassan, S. Algburi, A.Z. Sameen, H.M. Salman, M. Jaszczur, A review of hybrid renewable energy systems: Solar and wind-powered solutions: Challenges, opportunities, and policy implications, Results Eng. 20 (2023) 101621. https://doi.org/https://doi.org/10.1016/j.rineng.2023.101621.

[3] D. Siegmund, S. Metz, V. Peinecke, T.E. Warner, C. Cremers, A. Grevé, T. Smolinka, D. Segets, U.-P. Apfel, Crossing the Valley of Death: From Fundamental to Applied Research in Electrolysis, JACS Au. 1 (2021) 527–535. https://doi.org/10.1021/jacsau.1c00092.

[4] F. Lai, H. Shang, Y. Jiao, X. Chen, T. Zhang, X. Liu, Recent progress and perspective on electrocatalysis in neutral media: Mechanisms, materials, and advanced characterizations, Interdiscip. Mater. 3 (2024) 492–529. https://doi.org/https://doi.org/10.1002/idm2.12172.

[5] G. Gao, Z. Sun, X. Chen, G. Zhu, B. Sun, Y. Yamauchi, S. Liu, Recent advances in Ru/Ir-based electrocatalysts for acidic oxygen evolution reaction, Appl. Catal. B Environ. 343 (2024) 123584. https://doi.org/https://doi.org/10.1016/j.apcatb.2023.123584.

[6] M.N. Lakhan, A. Hanan, A. Hussain, I. Ali Soomro, Y. Wang, M. Ahmed, U. Aftab, H. Sun, H. Arandiyan, Transition metal-based electrocatalysts for alkaline overall water splitting: advancements, challenges, and perspectives, Chem. Commun. 60 (2024) 5104–5135. https://doi.org/10.1039/D3CC06015B.

[7] A.H. Al-Naggar, N.M. Shinde, J.-S. Kim, R.S. Mane, Water splitting performance of metal and non-metal-doped transition metal oxide electrocatalysts, Coord. Chem. Rev. 474 (2023) 214864. https://doi.org/https://doi.org/10.1016/j.ccr.2022.214864.

[8] L. Yu, J.F. Yang, B.Y. Guan, Y. Lu, X.W. (David) Lou, Hierarchical Hollow Nanoprisms Based on Ultrathin Ni-Fe Layered Double Hydroxide Nanosheets with Enhanced Electrocatalytic Activity towards Oxygen Evolution, Angew. Chemie Int. Ed. 57 (2018) 172–176. https://doi.org/https://doi.org/10.1002/anie.201710877.

[9] S. Zhao, M. Li, M. Han, D. Xu, J. Yang, Y. Lin, N.-E. Shi, Y. Lu, R. Yang, B. Liu, Z. Dai, J. Bao, Defect-Rich Ni3FeN Nanocrystals Anchored on N-Doped Graphene for

Enhanced Electrocatalytic Oxygen Evolution, Adv. Funct. Mater. 28 (2018) 1706018. https://doi.org/https://doi.org/10.1002/adfm.201706018.

[10] Q. Liu, P. Zhao, F. Zhao, J. Zhu, S. Yang, L. Chen, Q. Zhang, Bulk CrCoNiFe alloy with high conductivity and density of grain boundaries for oxygen evolution reaction and urea oxidation reaction, J. Colloid Interface Sci. 644 (2023) 1–9. https://doi.org/https://doi.org/10.1016/j.jcis.2023.04.055.

[11] H. Xie, Y. Zhang, P. Liu, X. Duo, Z. Hu, J. Yu, Z. Wang, G. Yao, L. Feng, X. Huang, R. Ouyang, Y. Wang, Rb-Doped Perovskite Oxides: Surface Enrichment and Structural Reconstruction During the Oxygen Evolution Reaction, Small. 20 (2024) 2400668. https://doi.org/https://doi.org/10.1002/smll.202400668.

[12] Z. Liu, F. Guo, L. Cheng, X. Bo, T. Liu, M. Li, Fabrication of manganese borate/iron carbide encapsulated in nitrogen and boron co-doped carbon nanowires as the accelerated alkaline full water splitting bi-functional electrocatalysts, J. Colloid Interface Sci. 629 (2023) 179–192. https://doi.org/https://doi.org/10.1016/j.jcis.2022.09.068.

[13] C. Liu, X. Chen, X. Zhang, J. Li, B. Wang, Z. Luo, J. Li, D. Qian, J. Liu, G.I.N. Waterhouse, Sodium Tartrate-Assisted Synthesis of High-Purity NiFe2O4 Nano-Microrods Supported by Porous Ketjenblack Carbon for Efficient Alkaline Oxygen Evolution, J. Phys. Chem. Lett. 14 (2023) 6099–6109. https://doi.org/10.1021/acs.jpclett.3c01244.

[14] L. Ma, Z. Wei, C. Zhao, X. Meng, H. Zhang, M. Song, Y. Wang, B. Li, X. Huang, C. Xu, M. Feng, P. He, D. Jia, Y. Zhou, X. Duan, Hierarchical superhydrophilic/superaerophobic 3D porous trimetallic (Fe, Co, Ni) spinel/carbon/nickel foam for boosting oxygen evolution reaction, Appl. Catal. B Environ. 332 (2023) 122717. https://doi.org/https://doi.org/10.1016/j.apcatb.2023.122717.

[15] X. Yu, G. Chen, Y. Wang, J. Liu, K. Pei, Y. Zhao, W. You, L. Wang, J. Zhang, L. Xing, J. Ding, G. Ding, M. Wang, R. Che, Hierarchical coupling effect in hollow Ni/NiFe2O4-CNTs microsphere via spray-drying for enhanced oxygen evolution electrocatalysis, Nano Res. 13 (2020) 437–446. https://doi.org/10.1007/s12274-020-2626-y.

[16] S. Möller, S. Barwe, J. Masa, D. Wintrich, S. Seisel, H. Baltruschat, W. Schuhmann, Online Monitoring of Electrochemical Carbon Corrosion in Alkaline Electrolytes by

Differential Electrochemical Mass Spectrometry, Angew. Chemie Int. Ed. 59 (2020) 1585–1589. https://doi.org/https://doi.org/10.1002/anie.201909475.

[17] F. Zoller, S. Häringer, D. Böhm, J. Luxa, Z. Sofer, D. Fattakhova-Rohlfing, Carbonaceous Oxygen Evolution Reaction Catalysts: From Defect and Doping-Induced Activity over Hybrid Compounds to Ordered Framework Structures, Small. 17 (2021) 2007484. https://doi.org/https://doi.org/10.1002/smll.202007484.

[18] A. Fujiwara, J. Wang, S. Hiraide, A. Götz, M.T. Miyahara, M. Hartmann, B. Apeleo Zubiri, E. Spiecker, N. Vogel, S. Watanabe, Fast Gas-Adsorption Kinetics in Supraparticle-Based MOF Packings with Hierarchical Porosity, Adv. Mater. 35 (2023) 2305980. https://doi.org/https://doi.org/10.1002/adma.202305980.

[19] M. Hammad, A. Amin, A. Asghar, O. Anwar, S. Salamon, J. Landers, M.-A. Kräenbring, A. Jain, S. Hardt, H. Wiggers, T.C. Schmidt, H. Wende, C. Schulz, D. Segets, Polyacrylic acid functionalized superparamagnetic iron-oxide supraparticles for highly efficient adsorption and removal of contaminants from water, J. Water Process Eng. 66 (2024) 106025. https://doi.org/https://doi.org/10.1016/j.jwpe.2024.106025.

[20] A. Amin, M. Loewenich, L. Grebener, M. Hammad, S. Heckenbach, M.-A. Kräenbring, A.S. Odungat, A.H. Ladole, T.B. Nguyen, D. Schwabenland, H.K. Salim, H. Wiggers, D. Segets, F. Özcan, Impact of Supraparticle Sizes and Morphology on Interparticle Spacing, Slurry Rheology, Coating Density, and Electrochemical Performance in Si/C Anodes for Li-Ion Batteries, (2025). https://doi.org/10.31224/4290.

[21] S. Wintzheimer, T. Granath, M. Oppmann, T. Kister, T. Thai, T. Kraus, N. Vogel, K. Mandel, Supraparticles: Functionality from Uniform Structural Motifs, ACS Nano. 12 (2018) 5093–5120. https://doi.org/10.1021/acsnano.8b00873.

[22] R.B. Ambade, H. Lee, K. Hyun Lee, H. Lee, G. Kumar Veerasubramani, Y.-B. Kim, T. Hee Han, Ultrafast flashlight sintered mesoporous NiO nanosheets for stable asymmetric supercapacitors, Chem. Eng. J. 436 (2022) 135041. https://doi.org/https://doi.org/10.1016/j.cej.2022.135041.

[23] A. and L. Amin Moritz and Kilian, Stefan O. and Wassmer, Theresa and Bade, Stefan and Lyubina, Julia and Wiggers, Hartmut and Özcan, Fatih and Segets, Doris, One-Step Non-Reactive Spray Drying Approach to Produce Silicon/Carbon Composite-Based Hierarchically Structured Supraparticles for Lithium-Ion Battery Anodes, J. Electrochem. Soc. (2023). http://iopscience.iop.org/article/10.1149/1945-7111/acb66b.

[24] P. Gerschel, S. Angel, M. Hammad, A. Olean-Oliveira, B. Toplak, V. Chanda, R. Martínez-Hincapié, S. Sanden, A.R. Khan, D. Xing, A.S. Amin, H. Wiggers, H. Hoster, V. Čolić, C. Andronescu, C. Schulz, U.-P. Apfel, D. Segets, Determining materials for energy conversion across scales: The alkaline oxygen evolution reaction, Carbon Energy. n/a (2024) e608. https://doi.org/https://doi.org/10.1002/cey2.608.

[25] A. Jain, C. Marcks, L. Grebener, J. Johny, A.S. Odungat, M. Chatwani, M.-A. Kräenbring, A. Shaji, M.F. Tesch, A.K. Mechler, V. Vinayakumar, D. Segets, A Proof-of-Principle Demonstration: Exploring the Effect of Anode Layer Microstructure on the Alkaline Oxygen Evolution Reaction, Adv. Funct. Mater. n/a (2025) 2421352. https://doi.org/https://doi.org/10.1002/adfm.202421352.

[26] V. Vinayakumar, T. Wagner, C. Marcks, J. Johny, G. Wartner, M.F. Tesch, I. Spanos, A. Ghafari, A. Jain, O. Prymak, I. Sanjuán, A.S. Odungat, O. Anwar, M. Chatwani, A. Jose, V. Chanda, A. Knop-Gericke, C. Andronescu, A.K. Mechler, N. Wöhrl, D. Segets, V. Vinayakumar, A. Jain, A.S. Odungat, O. Anwar, M. Chatwani, A. Jose, D. Segets, T. Wagener, N. Wöhrl, C. Marcks, A.K. Mechler, J. Johny, G. Wartner, M.F. Tesch, I. Spanos, A. Ghafari, A.K. Gericke, I. Sanjuán, V. Chanda, C. Andronescu, Ni-Co-O anodes for the alkaline oxygen evolution reaction: Multistage electrode optimization and plasma-assisted activity enhancement enabled by a coherent workflow, (2024). https://doi.org/10.31224/4205.

[27] D.K. Murugaiah, S. Shahgaldi, Recent progress in understanding the dispersion stability of catalyst ink for proton exchange membrane fuel cell and water electrolyzer, Int. J. Hydrogen Energy. 66 (2024) 156–169. https://doi.org/https://doi.org/10.1016/j.ijhydene.2024.04.036.

[28] K. Lam, Y. Gao, J. Wang, F. Ciucci, H2O2 Treated La0.8Sr0.2CoO3-δ as an Efficient Catalyst for Oxygen Evolution Reaction, Electrochim. Acta. 244 (2017) 139–145. https://doi.org/https://doi.org/10.1016/j.electacta.2017.05.083.

[29] Y. Miyahara, K. Miyazaki, T. Fukutsuka, T. Abe, Catalytic Roles of Perovskite Oxides in Electrochemical Oxygen Reactions in Alkaline Media, J. Electrochem. Soc. 161 (2014) f694–f697. https://doi.org/10.1149/2.019406jes.

[30] M. Hammad, S. Angel, A.K. Al-Kamal, A. Asghar, A. Said Amin, M.-A. Kräenbring, H.T.A. Wiedemann, V. Vinayakumar, M. Yusuf Ali, P. Fortugno, C. Kim, T.C. Schmidt, C.W.M. Kay, C. Schulz, D. Segets, H. Wiggers, Synthesis of novel LaCoO3/graphene

catalysts as highly efficient peroxymonosulfate activator for the degradation of organic pollutants, Chem. Eng. J. 454 (2023) 139900. https://doi.org/https://doi.org/10.1016/j.cej.2022.139900.

[31] S. Bapat, D. Segets, Sedimentation Dynamics of Colloidal Formulations through Direct Visualization: Implications for Fuel Cell Catalyst Inks, ACS Appl. Nano Mater. 3 (2020) 7384–7391. https://doi.org/10.1021/acsanm.0c01467.

[32] K. Kawashima, R.A. Márquez, Y.J. Son, C. Guo, R.R. Vaidyula, L.A. Smith, C.E. Chukwuneke, C.B. Mullins, Accurate Potentials of Hg/HgO Electrodes: Practical Parameters for Reporting Alkaline Water Electrolysis Overpotentials, ACS Catal. 13 (2023) 1893–1898. https://doi.org/10.1021/acscatal.2c05655.

[33] D. Segets, C. Lutz, K. Yamamoto, S. Komada, S. Süß, Y. Mori, W. Peukert, Classification of Zinc Sulfide Quantum Dots by Size: Insights into the Particle Surface–Solvent Interaction of Colloids, J. Phys. Chem. C. 119 (2015) 4009–4022. https://doi.org/10.1021/jp508746s.

[34] S. Brunauer, P.H. Emmett, E. Teller, Adsorption of Gases in Multimolecular Layers, J. Am. Chem. Soc. 60 (1938) 309–319. https://doi.org/10.1021/ja01269a023.

[35] J. Goworek, A. Borówka, S. Pikus, J. Wawryszczuk, Porosity of chemically modified silica gels by nitrogen adsorption, positron annihilation and small angle X-ray scattering, in: F. Rodriguez-Reinoso, B. McEnaney, J. Rouquerol, K.B.T.-S. in S.S. and C. Unger (Eds.), Charact. Porous Solids VI, Elsevier, 2002: pp. 655–662. https://doi.org/https://doi.org/10.1016/S0167-2991(02)80193-8.

[36] A. Jain, C. Marcks, L. Grebener, J. Johny, A.S. Odungat, M. Chatwani, M.-A. Kräenbring, A. Shaji, M.F. Tesch, A.K. Mechler, V. Vinayakumar, D. Segets, A Proof-of-Principle Demonstration: Exploring the Effect of Anode Layer Microstructure on the Alkaline Oxygen Evolution Reaction, (2024). https://doi.org/10.31224/4088.

[37] T. Koishi, K. Yasuoka, S. Fujikawa, T. Ebisuzaki, X.C. Zeng, Coexistence and transition between Cassie and Wenzel state on pillared hydrophobic surface, Proc. Natl. Acad. Sci. 106 (2009) 8435–8440. https://doi.org/10.1073/pnas.0902027106.

[38] F.-M. Chang, Y.-J. Sheng, S.-L. Cheng, H.-K. Tsao, Tiny bubble removal by gas flow through porous superhydrophobic surfaces: Ostwald ripening, Appl. Phys. Lett. 92 (2008) 264102. https://doi.org/10.1063/1.2953703.

[39] S. Herminghaus, Roughness-induced non-wetting, Europhys. Lett. 52 (2000) 165. https://doi.org/10.1209/epl/i2000-00418-8.

[40] A. Angulo, P. van der Linde, H. Gardeniers, M. Modestino, D. Fernández Rivas, Influence of Bubbles on the Energy Conversion Efficiency of Electrochemical Reactors, Joule. 4 (2020) 555–579. https://doi.org/https://doi.org/10.1016/j.joule.2020.01.005.

[41] M. Hammad, B. Alkan, A.K. Al-kamal, C. Kim, M.Y. Ali, S. Angel, H.T.A. Wiedemann, D. Klippert, T.C. Schmidt, C.W.M. Kay, H. Wiggers, Enhanced heterogeneous activation of peroxymonosulfate by Ruddlesden-Popper-type La2CoO4+δ nanoparticles for bisphenol A degradation, Chem. Eng. J. 429 (2022) 131447. https://doi.org/https://doi.org/10.1016/j.cej.2021.131447.

[42] M. Hammad, S. Angel, A.K. Al-kamal, A. Asghar, M.-A. Kräenbring, A. Amin, H.T.A. Wiedemann, A.S. Amin, V. Vinayakumar, T.C. Schmidt, C.W.M. Kay, D. Segets, H. Wiggers, Spray-flame synthesis of LaCo0.2Mn0.8O3 for selective peroxymonosulfate activation into singlet oxygen towards efficient degradation of carbamazepine, Process Saf. Environ. Prot. 194 (2025) 1347–1359. https://doi.org/https://doi.org/10.1016/j.psep.2024.12.060.

[43] Z. Xiao, Y.-C. Huang, C.-L. Dong, C. Xie, Z. Liu, S. Du, W. Chen, D. Yan, L. Tao, Z. Shu, G. Zhang, H. Duan, Y. Wang, Y. Zou, R. Chen, S. Wang, Operando Identification of the Dynamic Behavior of Oxygen Vacancy-Rich Co3O4 for Oxygen Evolution Reaction, J. Am. Chem. Soc. 142 (2020) 12087–12095. https://doi.org/10.1021/jacs.0c00257.

[44] D.A. Kuznetsov, M.A. Naeem, P. V Kumar, P.M. Abdala, A. Fedorov, C.R. Müller, Tailoring Lattice Oxygen Binding in Ruthenium Pyrochlores to Enhance Oxygen Evolution Activity, J. Am. Chem. Soc. 142 (2020) 7883–7888. https://doi.org/10.1021/jacs.0c01135.

[45] C.J. Anjeline, B.G. Marate, D. Velu, S.M.S. Kumar, N. Lakshminarasimhan, Probing oxygen vacancy-induced mixed-valence states of nickel in LaNiO3 and their influence on electrocatalytic and magnetic properties, Mater. Chem. Phys. 288 (2022) 126331. https://doi.org/https://doi.org/10.1016/j.matchemphys.2022.126331.

[46] J. Diao, W. Yuan, Y. Qiu, L. Cheng, X. Guo, A hierarchical oxygen vacancy-rich WO3 with “nanowire-array-on-nanosheet-array” structure for highly efficient oxygen evolution reaction, J. Mater. Chem. A. 7 (2019) 6730–6739.

https://doi.org/10.1039/C9TA01044K.

[47] K. Zhu, T. Wu, M. Li, R. Lu, X. Zhu, W. Yang, Perovskites decorated with oxygen vacancies and Fe–Ni alloy nanoparticles as high-efficiency electrocatalysts for the oxygen evolution reaction, J. Mater. Chem. A. 5 (2017) 19836–19845. https://doi.org/10.1039/C7TA05404A.

[48] H. Sun, Y. Zhao, K. Mølhave, M. Zhang, J. Zhang, Simultaneous modulation of surface composition, oxygen vacancies and assembly in hierarchical Co3O4 mesoporous nanostructures for lithium storage and electrocatalytic oxygen evolution, Nanoscale. 9 (2017) 14431–14441. https://doi.org/10.1039/C7NR03810K.

[49] H. Geng, X. Zou, Y. Min, Y. Bu, Q. Lu, Advances and Challenges in Perovskite Oxide Design for High-Performance Zinc–Air Batteries: Integrating Experimental Strategies and Machine Learning, Adv. Funct. Mater. n/a (2025) 2500657. https://doi.org/https://doi.org/10.1002/adfm.202500657.

[50] L. Zhuang, L. Ge, Y. Yang, M. Li, Y. Jia, X. Yao, Z. Zhu, Ultrathin Iron-Cobalt Oxide Nanosheets with Abundant Oxygen Vacancies for the Oxygen Evolution Reaction, Adv. Mater. 29 (2017) 1606793. https://doi.org/https://doi.org/10.1002/adma.201606793.

[51] X. Wang, C. Xing, Z. Liang, P. Guardia, X. Han, Y. Zuo, J. Llorca, J. Arbiol, J. Li, A. Cabot, Activating the lattice oxygen oxidation mechanism in amorphous molybdenum cobalt oxide nanosheets for water oxidation, J. Mater. Chem. A. 10 (2022) 3659–3666. https://doi.org/10.1039/D1TA09657E.

[52] A. Vazhayil, L. Vazhayal, J. Thomas, S. Ashok C, N. Thomas, A comprehensive review on the recent developments in transition metal-based electrocatalysts for oxygen evolution reaction, Appl. Surf. Sci. Adv. 6 (2021) 100184. https://doi.org/https://doi.org/10.1016/j.apsadv.2021.100184.

[53] F. Wang, P. Zou, Y. Zhang, W. Pan, Y. Li, L. Liang, C. Chen, H. Liu, S. Zheng, Activating lattice oxygen in high-entropy LDH for robust and durable water oxidation, Nat. Commun. 14 (2023) 6019. https://doi.org/10.1038/s41467-023-41706-8.